UC San Diego

UC San Diego Electronic Theses and Dissertations

Title

Reversing the Coffee-Ring Effect for Enrichment in Diagnostic Assays

Permalink

https://escholarship.org/uc/item/63370453

Author

Wang, Edward

Publication Date

2023

Peer reviewed|Thesis/dissertation

UNIVERSITY OF CALIFORNIA SAN DIEGO

Reversing the Coffee-Ring Effect for Enrichment in Diagnostic Assays

A dissertation submitted in partial satisfaction of the
requirements for the degree
Doctor of Philosophy

in

Materials Science and Engineering

by

Edward Wang

Committee in charge:

Professor Yu-Hwa Lo, Chair
Professor Ratneshwar Lal
Professor Louise Laurent
Professor Darren Lipomi
Professor Tse Nga Ng

2023

The Dissertation of Edward Wang is approved, and it is acceptable in

quality and form for publication on microfilm and electronically:

University of California San Diego

2023

Table of Contents

List of Figures

Acknowledgments

I would like to thank my advisor Prof. YuHwa Lo for his support our thoughtful discussions during each of my research projects, as well as my committee members: Dr. Ratneshwar Lal, Dr. Louise Laurent, Dr. Darren Lipomi, and Dr. Tina (Tse Nga) Ng for their guidance throughout my graduate career.

I also appreciate the helpful environment fostered members of the Lo Research group, including Wei Cai, Chi-Yang Tseng, Alex Zhang, Xinyu Chen, Lauren Waller, Zhilin Guo, Rui Tang and Zunming Zhang, who have all been pivotal for my development as both a researcher and person over these past few years.

The material in this dissertation is based on the following published papers:

Chapter 2 is based on the following paper, . E. Wang, Z. Guo, R. Tang and Y. H. Lo, Using airflow-driven, evaporative gradients to improve sensitivity and fluid control in colorimetric paper-based assays, Lab Chip, 2021, 21, 4249–4261.

Chapter 3 is based on the following paper, E. Wang, L. C. Laurent, D. A. Hall and Y. H. Lo, Sample preconcentration through airjet-induced liquid phase enrichment, Lab Chip, 2023, 23, 4033–4043

Vita

Education

2017   Bachelor of Science in Biochemistry, University of Illinois at Urbana-Champaign

2018   Master of Science in Materials Science and Engineering, University of California San Diego

2023   Doctor of Philosophy in Materials Science and Engineering, University of California San Diego

Publications

1. **E. Wang**, L. C. Laurent, D. A. Hall and Y. H. Lo, Sample preconcentration through airjet-induced liquid phase enrichment, *Lab Chip*, 2023, **23**, 4033–4043.

2. **E. Wang**, Z. Guo, R. Tang and Y. H. Lo, Using airflow-driven, evaporative gradients to improve sensitivity and fluid control in colorimetric paper-based assays, *Lab Chip*, 2021, **21**, 4249–4261.

3. W. Cai, E**. Wang**, P.-W. Chen, Y.-H. Tsai, L. Langouche and Y.-H. Lo, Using airflow-driven, evaporative gradients to improve sensitivity and fluid control in colorimetric paper-based assays, *Biomicrofluidics*, 2019, **13**, 024109.

4. L. Waller, Z. Guo, R. Tang, Z. Zhang, **E. Wang**, J. Yasuhara-Bell, L. Laurent and Y. H. Lo, High Sensitivity, Rapid Detection of Virus in High Traffic Environments, *Front. Bioeng. Biotechnol.*, 2022, **10**, 877603.

5. S. Vijayakumar, S. H. Nasr, J. E. Davis, **E. Wang**, J. M. Zuidema, Y. S. Lu, Y. H. Lo, J. K. Sicklick, M. J. Sailor and P. Ray, Anti-KIT DNA aptamer-conjugated porous silicon nanoparticles for the targeted detection of gastrointestinal stromal tumors, *Nanoscale*, 2022, **14**, 17700–17713.

Abstract of the Dissertation

Reversing the Coffee-Ring Effect for Enrichment in Diagnostic Assays

By

Edward Wang

Doctor of Philosophy in Materials Science and Engineering

University of California San Diego, 2023

Professor Yu-Hwa Lo, Chair

The coffee-ring effect (CRE) is a common occurrence in drying droplets, characterized by the formation of a ring-like deposit around the droplet's edge due to differential evaporation rates. This phenomenon is widely observed in various applications, including enhancing detection in biological assays, where researchers have explored ways to utilize the CRE to improve analyte concentration. Reversing the CRE becomes crucial as it enables the

concentration of biological analytes at the droplet's center, thereby enhancing detection sensitivity in subsequent assays. In this work, we discuss a simple method to reverse the CRE using airflow, creating a reverse evaporative gradient, and providing a potential solution for improving sensitivity in bioassays.

The initial study focuses on utilizing the evaporative enrichment method to control fluid flow for solutes in liquids. The general principle of reversing the evaporative gradient is demonstrated through use of an IR laser, then accomplished in simpler terms using airflow. The simplicity and adaptability of this technique are showcased through applications in colorimetric detection of proteins and nucleic acids on paper in point of care settings. By employing airflow, the colorimetric substance can be concentrated, mitigating its uniform distribution. This concentration allows for the formation of distinct spot morphologies on the paper, enabling more precise detection of analytes compared to traditional methods.

The next part of work explores the capabilities and implementation of the airflow method to concentrate various particles and biological analytes in liquid samples. Model analytes, such as λ-DNA, HeLa-S3 RNA, and heat-inactivated SARS-CoV-2, were included in spiked samples to assess the resulting reduction in cycle threshold values in PCR analysis. Additionally, co-enrichment of PEG was applied as a sample pre-treatment method to minimize interference from salt accumulation in downstream analysis. While the integration of airflow enrichment was initially explored in microfluidic systems, the method was also scaled up to larger volumes to assess its efficacy in common laboratory practices related to PCR-based detection.

Chapter 1 Reversal of the Coffee-Ring Effect via Infrared Laser

1.1 Overview

The performance of sensors for organic and inorganic chemical compounds, DNAs, proteins, virus, bacteria, etc. are often measured by the minimum concentration of the target particles the sensors can detect. Hence sample enrichment in solution phase is usually a necessary step in the work flow of sample process. Today's sample enrichment methods are mostly material specific, utilizing the unique physical, chemical, and biological properties of the target particles. The methods usually involve sample capturing process, followed by sample release. For example, the target particles are captured by flowing samples through a column of high surface area having strong affinity with the target particles. Then the captured particles are released into the elusion buffer.(1–5) Such processes of sample enrichment and extraction require multiple steps and have limited throughputs.

Besides using chemical properties of binding affinity, there have been numerical approaches using physical properties of particles for enrichment. These approaches use passive or active devices based on the mechanisms that control the motions of particles in the sample solution. Passive designs can use Van der Waals attraction(6), Brownian motion(7) and charged dipole interaction(8). Active designs make use of hydrodynamic force(9–12), dielectrophoretic (DEP) effect(13–15), electrophoretic (EP) effect(16,17), magnetophoretic effect(18,19) and thermophoretic(20–22). The DEP device and operation conditions (e.g. electric signal frequencies) need to be adjusted to work for certain particles based on their Clausius–Mossotti (CM) factor, which determines whether the particles moved towards or away from the electric field gradient. The device design and operation condition also depend critically on the particle

2

volume and the ionic strength of buffer. Hence DEP devices work more effectively for larger particles such as bacteria and mammalian cells(25,26). In contrast, device using electrophoretic (EP) effect works more effectively with smaller particles such as proteins and nucleic acids. While the EP effect has been widely established with gel electronics to separate charged biomolecules, the technique is often used for molecular analyses such as western blot (for proteins) and southern blot (for DNAs) instead of sample enrichment for applications such as in-vitro diagnosis (IVD) and point-of-care. Thermophoresis can be used to trap DNAs in a microscopic volume through convection induced by temperature gradient(23). Since particles tend to move from hot areas to cold areas against the thermal gradient, normally thermophoretic effect causes depletion rather than accumulation of particles near the heat source. However, by adjusting the chamber thickness to tailor the thermal gradient across the chamber and by controlling the salt concentration, particle enrichment can occur near the hot spot. Using this technique, SYBR-stained DNA in the solution is enriched from an initial concentration of 0.5 nM to uM concentration range in 3 minutes, giving rise to an enrichment factor of over 1000.

To summarize, almost all existing sample enrichment methods are designed for specific types of particles according to the chemical and electrical properties of particles and the pH value and ionic strength of the solution. The enrichment method requires either special reagents or specific device design such as device geometry, electrode patterning, surface functionalization, etc.. From cost and efficiency concerns, it is desirable to develop an effective and efficient method that can enrich bioparticles of any properties and size, including proteins, nucleic acids, cell secreted particles such as exosomes and micro vesicles, virus, bacteria, and mammalian cells. In this paper, we report a sample enrichment method using differential mass transport by CO_2 laser induced evaporation. Utilizing the strong water absorption at the CO_2

3

wavelength (10.6 μm), we create a strong differential evaporation rate over the sample containing chamber with the highest evaporation rate at the laser focal spot. The differential evaporation rate generates a net flow of any suspended particles due to the effect of mass transport, which far exceeds any diffusion effect due to thermal gradient. As a result, all suspended particles in the sample, no matter where they are and regardless their solubility, are driven towards the local spot defined by the CO_2 laser spot, producing a greatly enhanced particle concentration tracing the position of the laser spot. In a simple analogy to explain how the method works, one can envision the CO_2 laser spot as the drain of a reservoir. Even if water continues to be added to the reservoir to balance the water loss through the drain, the differential rate of water loss creates mass transport that drives all suspended particles in the reservoir towards the position of the drain. This method has the following salient features suitable for sample enrichment for biosensing and biological sample process: (1) the method works for particles of any size, shape, and physical and chemical properties, (2) the method can handle a wide range of initial particle concentration, (3) the method does not require any device processing such as formation of electrodes, microfluidic devices, or surface functionalization (e.g. control of hydrophobicity, surface charge control, specific capturing probes, etc.), and (4) having the CO_2 laser illuminate the sample solution from the bottom, the method offers a completely open platform, as opposed to a closed system found in most sample enrichment devices, to allow convenient monitoring and accessibility for changing, adding, or replenishing the sample solution any time during the action. In the following we describe the experimental setup, the proof-of-concept experiments, and theoretical analysis and simulations of the method.

1.2 CO2 laser setup and enrichment effect

The CO2 laser system is specifically engineered to induce mass transport, enhancing the solute concentration in the liquid medium. Figure 1.1 depicts the experimental setup: a 10 W CO2 laser (Universal Laser Systems ULR-10) emitting light at a wavelength of 10.6 μm is used as the heat source. The laser produces a nearly collimated output with a beam width of 4 mm and a divergence angle of 5 mrad. Laser power modulation occurs at 20 kHz, and the output power is controlled by varying the duty cycle from 0 to 100%. To initiate mass transport, the laser beam is expanded tenfold using a beam expander comprising a pair of plano-concave (focal length -50 mm, diameter 1″) and plano-convex (focal length 500 mm, diameter 1″) zinc selenide (ZeSe) lenses, coated with a broadband (7 - 12 μm) antireflective coating. The expanded laser beam, now 40 mm in diameter, is directed towards the sample's bottom via a 45° angle gold-coated mirror. The beam is further focused into a 30 μm spot on the sample solution's bottom using a plano-convex (focal length 50 mm, diameter 1″) ZeSe lens and a thin cover glass slide. For excitation, either a 488 nm or 406 nm laser fiber is utilized based on the fluorescence properties of the solute or particles. The excitation laser light is collimated, reflected by a 505 nm long pass dichroic mirror, and then passes through a 20X objective lens. Subsequently, emitted light is collected back through the same objective lens, transmitted through the 505 nm long pass dichroic mirror, and detected by a CCD camera.When the laser is turned on, the solute in the solution moves towards the laser spot by mass transport as illustrated in **Figure 1.2.**
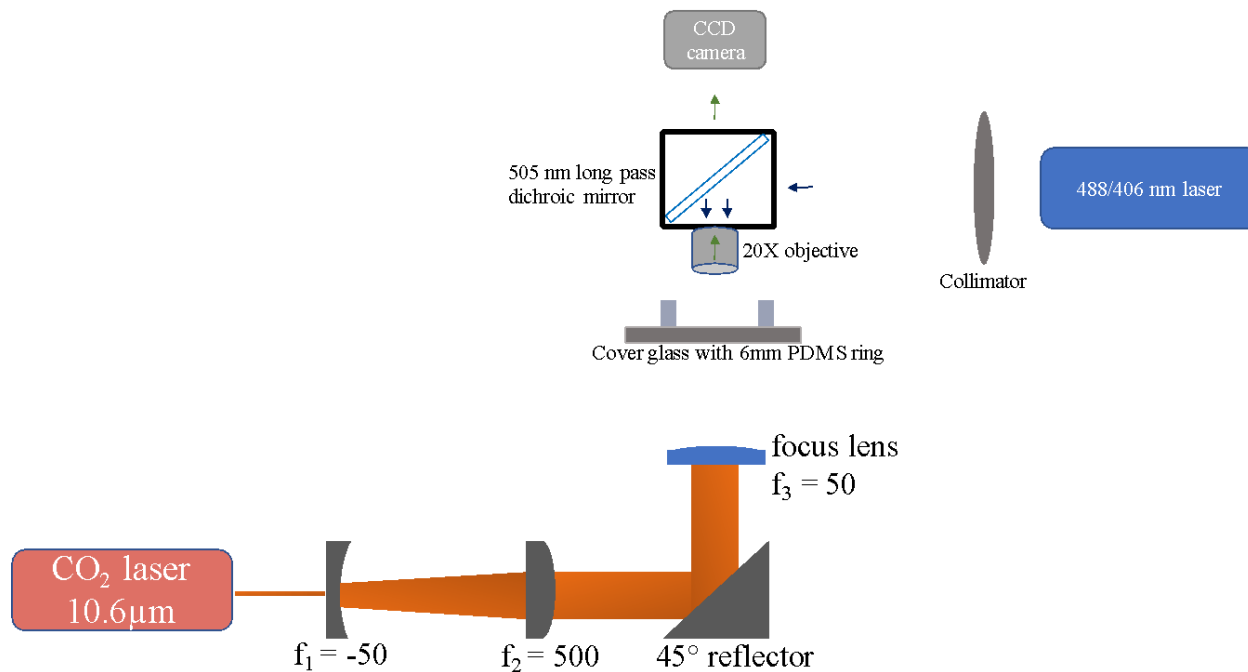
Figure 1.1 Schematic of the experimental setup
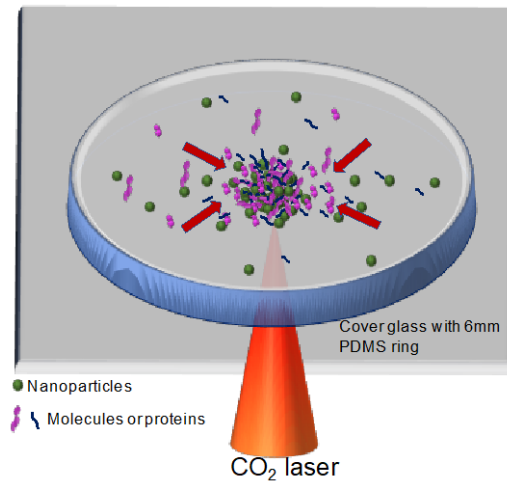
Figure 1.2 The operation principle of CO_2 laser induced enrichment

To illustrate the mass transport effect initiated by the laser, an 8 μL sample containing 1 μM of

fluorescent single-stranded DNA (ssDNA) labeled with FAM dye, measuring 90 nucleotides in

length, was introduced into a chamber with PDMS walls and a bottom surface made of cover

glass. As depicted in **Figure 1.3**, the fluorescent intensity profile of the FAM-labeled ssDNA

was tracked over time. Enrichment commenced approximately 60 seconds after laser irradiation,

and the concentration escalated exponentially, signifying the dominance of the mass transport

effect in guiding the movement of DNAs within the sample solution.

In **Figure 1.3(a)**, the fluorescent intensity profile plateaus due to the saturation of the

CCD camera, yet the enrichment process continues. The laser's estimated absorbed power by the

sample amounted to around 40 mW, resulting in an evaporation rate of 1 μL/min. Figure 1.3(b)

displays representative images depicting the distribution of fluorescent intensity after laser

irradiation for 90 s, 120 s, and 180 s, respectively.
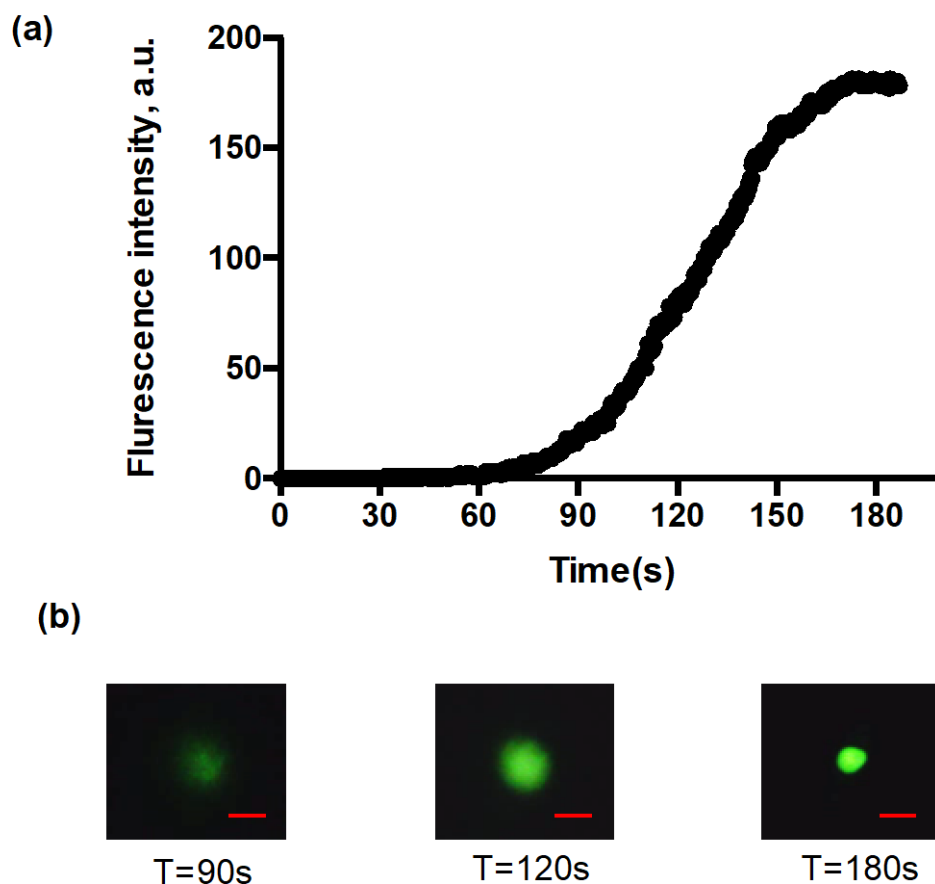
Figure 1.3 Fluorescent ssDNA enrichment profile. (a) Fluorescence intensity change over time. The intensity saturation after 150 seconds is due to the dynamic range limit of the CCD camera. (b) Representative images showing the spatial distribution of the fluorescent ssDNA at t = 90 s; t = 120 s and t = 180 s, respectively. The scale bar is 200 μm.

To quantitatively study the enrichment power of the method, a series of experiments with different initial DNA concentrations from 100 nM to 10 pM in 8 μL solution were analyzed. **Figure 1.4** shows the enrichment profile of each initial DNA concentration after 4 minutes of CO_2 laser irradiation. The camera exposure time was controlled and any nonlinear response of the CCD camera was removed to relate the camera output to the DNA concentration. The enrichment factor is obtained from the comparison between the peak intensity of the enriched sample and the background intensity of a pre-enriched sample of higher DNA concentration. For

instance, as the maximum fluorescent intensity for a 10 pM sample after enrichment matches that

of a 1 μM DNA sample without enrichment, we determine that the enrichment factor is 100,000.

The intensity profile also produces the DNA concentration profile in the solution.
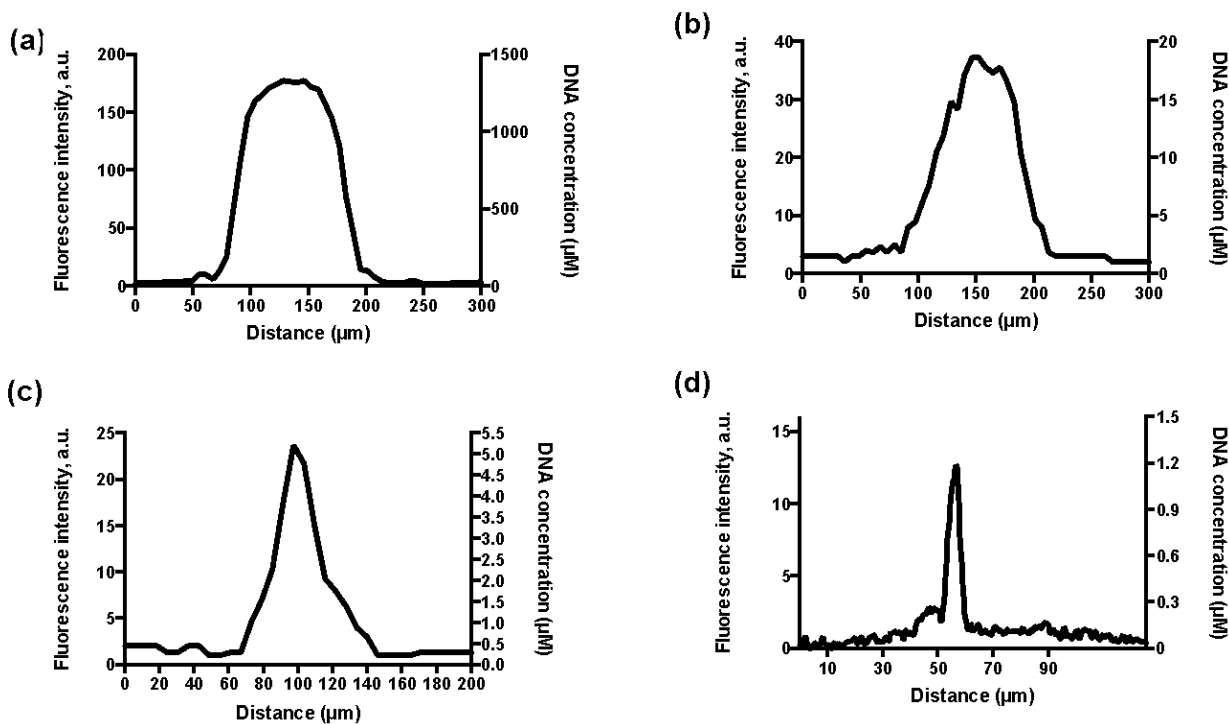
Figure 1.4 Fluorescent DNA profile with different initial concentrations (a) 100 nM, (b) 10 nM, (c) 100 pM, (d) 10 pM. All data are taken after 4 minutes of CO_2 laser irradiation. The *y*-axes show both the fluorescent intensity (left) from calibrated CCD output signal and the actual DNA concentration profile (right).

The CO2 laser-induced enrichment method offers distinct advantages for sample

enrichment in biosensing and biological sample processes. Firstly, it is versatile, accommodating

particles of any size, shape, and chemical composition. Secondly, it can handle a wide range of

initial particle concentrations, providing flexibility in sample analysis. Importantly, it does not

require complex device processing, such as electrode formation or surface functionalization,

simplifying the experimental setup. Unlike most sample enrichment devices, this method utilizes

a CO2 laser to illuminate the sample solution from the bottom, creating an open platform. This

9

openness allows easy monitoring and accessibility for modifying, adding, or replenishing the sample solution during the process.

An application of this method involved the formation of aggregates, illustrated in **Figure 1.5 (a)**. In this experiment, MCF7/GFP cells were cultured in exosome-free medium, and the exosome secretion rate was determined. Biotinylated exosomes were formed by incubating the conditioned medium with specific antibodies. A solution containing 4 µL of biotinylated exosomes and 4 µL of 40 pM 25 nm streptavidin Q-dots was dispensed onto the device, with an 8 µL Q-dots-only solution used as a control. After 4 minutes of CO_2 laser irradiation, as depicted in **Figure 1.5 (b)-(c)**, both the Q-dots and exosomes in both solutions were concentrated at the laser center. Upon turning off the CO_2 laser, the Q-dots rapidly diffused out in the control experiment **(Figure 1.5 (b))**. In the sample with biotinylated exosomes, the formation of aggregates caused only the unbound Q-dots to diffuse out, allowing fluorescence to be observed even 3 minutes after the laser was turned off **(Figure 1.5 (c))**. This highlights the effectiveness of

the method in retaining specific particles during the enrichment process.
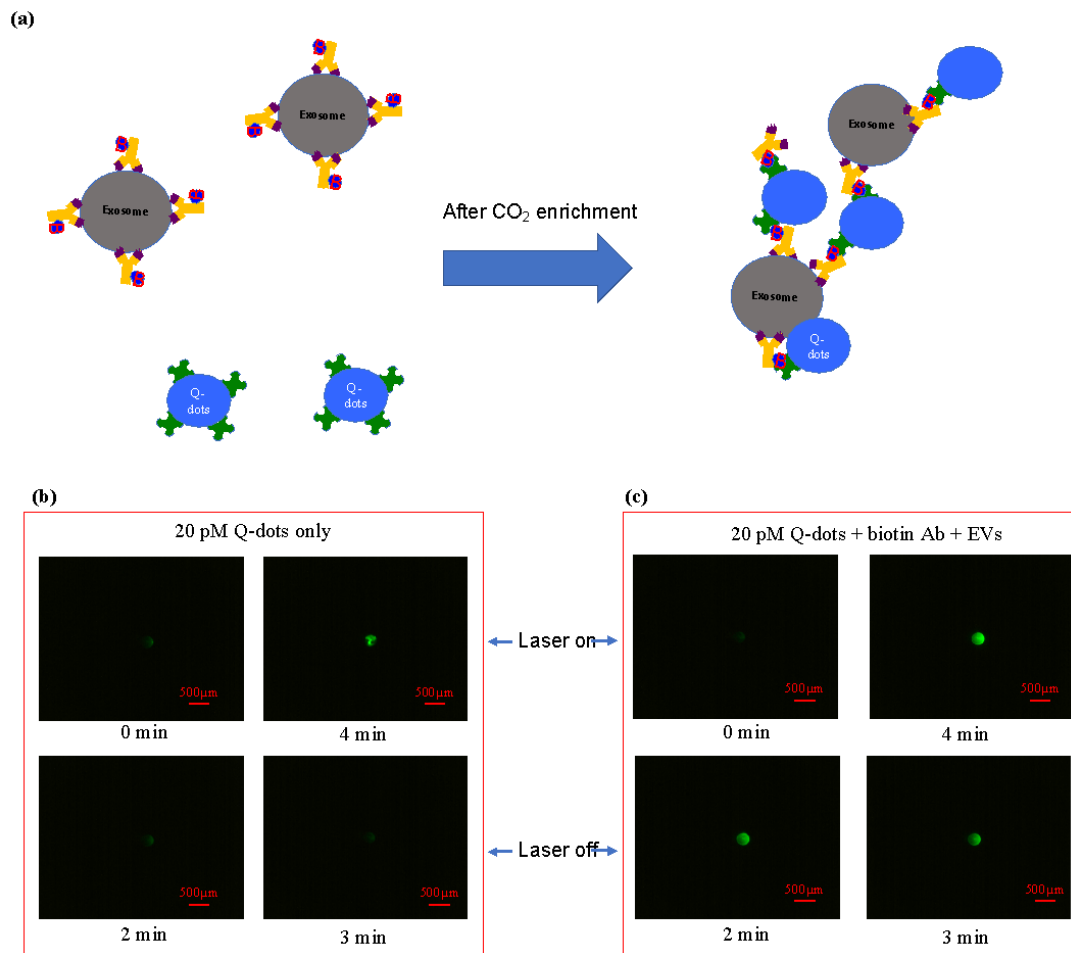
Figure 1.5 (a) The schematic of the formation of aggregates. (b) 20 pM streptavidin Q-dots enriched by CO_2 laser; (b) Aggregation formation with CO_2 laser

      While the laser-induced differential evaporation rates lead to mass transport toward the laser spot, they also create a distinct temperature profile. Although measuring the evaporation rate profile directly is challenging, we can obtain relevant data by examining the temperature profile using a thermal imager (A325sc from FLIR). This temperature profile is particularly crucial for biological samples like DNAs and proteins. In our experiment, a 40 mW CO2 laser, focused to a 30 μm spot, raises the spot temperature from 25 ℃ to 58.5 ℃ within 10 seconds. Simultaneously, diffusion and convection effects increase the temperature of the surrounding

area (within a diameter of 3 millimeters) to 42 °C, resulting in a net evaporation rate of 1 μl/min. **Figure 1.6 (b)** illustrates the evolving temperature profile during the initial 60 seconds of CO2 laser irradiation, after which the temperature profile reaches steady state.

Using the temperature profile (**Figure 1.6**) and the relation between temperature and evaporation rate, the evaporation rate profile can be produced (**Figure 1.7**).

Water evaporation rate per area is calculated as:

$$E = \theta * (X_s - X) \qquad (1\text{-}1)$$

$$\theta = 25 + 19 * v \qquad (1\text{-}2)$$

where θ is the evaporation coefficient, v is the velocity of air above the sample surface which we assumed to be 0 in our calculation. X is the humidity ratio in air[59]. Based on the Ideal Gas Law, the humidity ratio can be represented as

$$X = 0.62198 * \frac{P_w}{(P_a - P_w)}) \qquad (1\text{-}3)$$

P_w is the partial pressure of water vapor in moist air and P_a is atmospheric pressure of 101,325 Pa. X_s is the maximum humidity ratio of humidity saturated air of the same temperature as the sample surface.

$$X_s = 0.62198 * \frac{P_{ws}}{(P_a - P_{ws})}) \qquad (1\text{-}4)$$

According to Antoine equation, saturated pressure of water vapor can be expressed as:

$$P_{ws} = \frac{e^{(77.345 + 0.0057 * T - \frac{7235}{T})}}{T^{8.2}} \qquad (1\text{-}5)$$

The humidity is

$$\emptyset = \frac{P_w}{P_{ws}} * 100\% \qquad (1\text{-}6)$$

The evaporation rate reaches the maximum value at the center area, due to its highest surface temperature. The following Computational Fluid Dynamics (CFD) computations will demonstrate that the mass transport via the differential evaporation rate is key to sample enrichment. It should also be noted that the evaporation rate is highly correlated with the humidity in the air phase. As humidity decreases, the evaporation rate increases and thus subsequently affects the enrichment process.
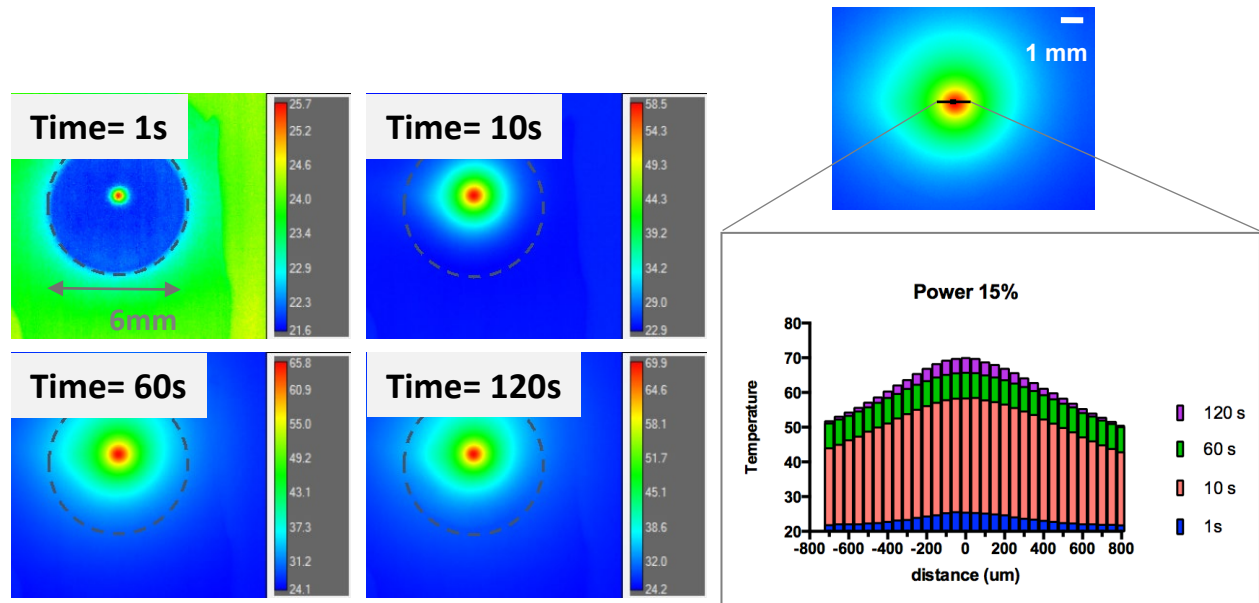
Figure 1.6 (a) Temperature heat map for different CO_2 laser irradiation time periods: 1 s, 10 s, 60 s and 120 s. (b) Temperature profiles under different durations of CO_2 laser irradiation.
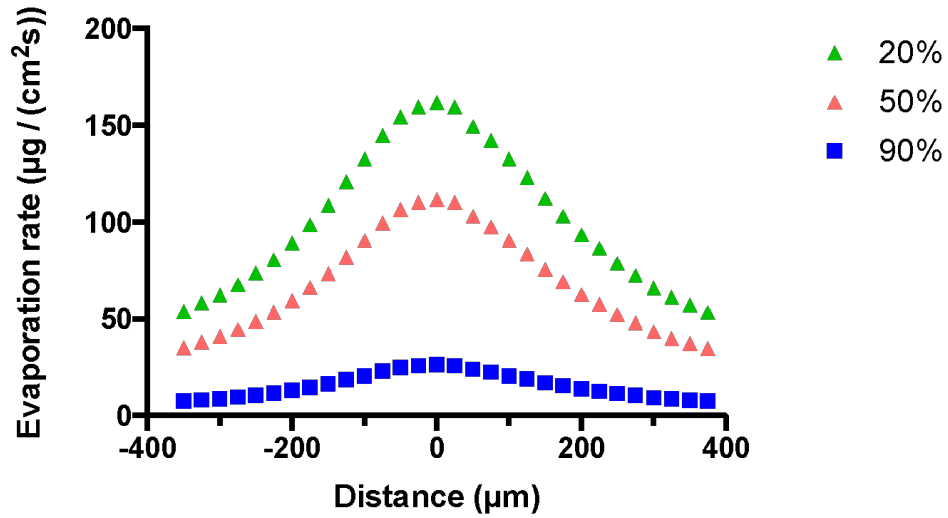
Figure 1.7 Calculated sample evaporation rate profile at 20%, 50%, 90% relative humidity using the temperature profile at 120 s in Figure 1.5

1.3 CFD Simulations

To elucidate the experimental results of laser-induced enrichment, CFD simulations were performed to provide insights on the fluid flow, which is critical to the differential mass transport by CO_2 laser induced evaporation.

1.3.1 Governing Equations

The liquid evaporation with laser heating can be modeled with two-phase laminar flow using Arbitrary Lagrangian Eulerian moving mesh method in the axisymmetric three dimensional cylinder coordinate.
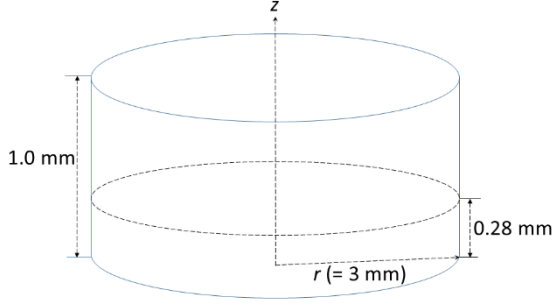
Figure 1.8 Schematics of the water-vapor system. The laser is applied at the central of the bottom surface.

The governing equations incorporate mass, momentum and heat transfer coupled with interfacial evaporation with the aid of local laser-heating. The Navier-Stoke equation is solved along with continuity equation of compressibility to compute velocities of laminar flows for water liquid phase and vapor phase,

$$\rho\left[\frac{\partial u}{\partial t} + (u \cdot \nabla)u\right] = \nabla \cdot \left[-p \cdot I + \mu(\nabla u + \nabla u^T) - \frac{2}{3}\mu(\nabla \cdot u)I\right] + F \qquad (1\text{-}1)$$

$$\frac{\partial \rho}{\partial t} + \nabla \cdot (\rho u) = 0 \qquad (1\text{-}2)$$

where ρ is the density; μ represents the viscosity; p is the pressure; and F is the volume force arisen from the gravity. The temperature profile inside the water phase and the vapor phase are simulated with the heat transfer equation, which consists of heat convention and conduction,

$$\rho C_p \frac{\partial T}{\partial t} + \rho C_p u \cdot \nabla T + \nabla \cdot (-k\nabla T) = 0 \qquad (1\text{-}3)$$

where T is temperature, C_p represents heat capacity; and k stands for water heat conductivity. The momentum and heat transfer equations are solved for coupled gas and liquid phases. The mass transfer inside the vapor phases is expressed in terms of convection and diffusion,

$$\frac{\partial c}{\partial t} + (u \cdot \nabla)c - \nabla \cdot (D\nabla c) = 0 \qquad (1\text{-}4)$$

15

where c and t stand water molar concentration and time respectively; $\boldsymbol{u}$ is the velocity, obtained from momentum equation; and D is the diffusion coefficient.

1.3.2 Initial Conditions

The initial condition for the vapor domain is the ambient temperature, T_0 (= $293.15\ K$), and the relative humidity X_h is 30%, then initial water concentration, $c_{w0}^v = c_{w0}^{sat} * X_h$ is calcuated according to ideal gas equation of state. The initial saturated concentration c_{w0}^{sat} at the ambient temperature is also calculated as, P_{sat}/RT, where the saturated steam pressure is estimated with the Antoine equation. All other physical properties such as density, viscosity and diffusivities are evaluated at ambient temperature and pressure (p_0= $1\ atm$). The initial velocities in the vapor and the liquid phase are assigned as zero.

1.3.3 Boundary Conditions

In the boundary conditions, for the momentum transfer in the vapor phase, the open boundary with constant pressure is given at the top part of vapor phase,

$$p = 0\ atm, \qquad \text{at } z = 0.6\ mm \qquad (1\text{-}5)$$

where p is the dynamic pressure, total pressure $p_{total} = p_0 + p$. At the PDMS-water interface, a slip wall is adopted and a constant PDMS-air-water contact angle, $\Theta_w = 110^o$, is assigned to compute surface effect,

$$\gamma_{sl} - \gamma_{sv} = \sigma_{lv} cos\theta_w \qquad (1\text{-}6)$$

where γ_{sl}, γ_{sv} and σ are surface energy density for surface-lipid, surface-vapor, and surface tension for liquid-vapor interfaces respectively. In the simulation, the temperature-

dependent σ_{lv} was adopted from literature. The whole PDMS side wall is slippery with zero normal velocity; and the bottom of container is simply no flow conditions.

$$n \cdot u = 0, \quad \text{at } r = 3.0 \text{ mm} \tag{1-7}$$

$$u=0, \quad \text{at } z=0 \text{ mm} \tag{1-8}$$

where r is the cylindrical r-coordinate.

For the mass transfer in the vapor phase, the outer condition is given at the top part of the vapor phase ($z = 0.6$ mm).

$$c = c_{w0}^v, \text{ if } n \cdot u < 0 \tag{1-9}$$

$$-n \cdot q = 0, \text{ if } n \cdot u \geq 0 \tag{1-10}$$

At the lipid-vapor interface, the mass flux condition $\dot{m}_e$ is applied,

$$-n \cdot q = \dot{m}_e \tag{1-11}$$

$$\dot{m}_e = k_e(c_w^{sat} - c_w^v) \tag{1-12}$$

where c_w^{sat} and c_w^v represent instantaneous saturation water concentration and water vapor concentration respectively; and k_e (=0.02 (1/s)) stands for the mass transfer rate between liquid and vapor phases. At the PDMS side wall, there is no mass flux,

$$\frac{\partial c}{\partial z} = 0, \quad \text{at } r = 3 \text{ mm and } z = 0 \text{ mm (if interface touches bottom)} \tag{1-13}$$

For the heat transfer, the outer boundary is adopted for the upper part of the vapor phase ($z = 0.5$ mm),

$$T = T_0, \quad \text{if } n \cdot u < 0 \tag{1-14}$$

$$-n \cdot q = 0, \quad \text{if } n \cdot u \geq 0 \tag{1-15}$$

At the lipid-vapor interface, the heat conservation is reserved,

$$\rho C_p \frac{\partial T}{\partial t} + \rho C_p u \cdot \nabla T + \nabla \cdot (-k\nabla T) = Q_e \qquad \text{(1-16)}$$

$$Q_e = -h_e m_{eWe} \qquad \text{(1-17)}$$

where h_e is water latent heat (J/kg), which is determined by the instantaneous temperature. At the bottom part of the water phase, there is heat supply ($Q_p = 0.04\ W$) at the central part of the bottom surface,

$$-n \cdot q = Q_p, \quad \text{at } r \leq 100\ \mu m,\ z{=}0 \qquad \text{(1-18)}$$

It should be noted although Q_p is assigned at the bottom of the surface, if the grid mesh is considered, Q_p is applied on a grid with the length of 15 μm.

For the other area of the bottom surface (at $z = 0.0\ mm$ and $r > 150\ \mu m$) or the PDMS side wall ($r = 3.0\ m$), heat insulation condition is applied.

$$-n \cdot q = 0, \qquad \text{(1-19)}$$

The partial differential equations were solved with COMSOL multiphysics software (Version 5.2, COMSOL Inc. USA).

The simulation results show two main effects that cause water to flow: thermocapillary convection and differential evaporation. Previous studies showed that natural convection is strongly suppressed in comparison with thermocapillary conversion for a small system with length less than a few millimeters[45]. Thermocapillary convection is resulted from a surface tension gradient due to the temperature profile in the fluid since surface tension is reduced with increasing temperature.

Figure 1.9 shows the simulated water velocity profile at different times (12 s and 322 s) after the CO_2 laser is turned on. At positions far from the center, water flows from the PDMS boundary of the reservoir towards the center by taking a path near the bottom surface. When the

flow reaches some distance from the center, the flow direction turns upward, driven by two mechanisms: thermocapillary effect and differential evaporation. The thermocapillary effect circulates a part of the flow back by taking a path near the liquid surface, forming a convection flow. On the other hand, another part of the flow that is very close to the center (e.g. within 100 μm from the center) takes a different path than the thermocapillary convection flow. Instead of circulating back, it reaches the liquid surface and evaporates.

The flow velocity profile helps envision how particles behave in the liquid. The particles will follow the flow path and, at the same time, experience random (Brownian) motions. They also experience interparticle interactions under certain concentration and local environment. Ignoring the Brownian motions and interparticle interactions, particles will be either accumulated at the surface where water evaporates or circle around following the path of thermocapillary convection. For those particles circulating around, over time their Brownian motions can bring them to the flow path that ends at the center area dominated by evaporation. Once the particles are accumulated at the surface, they are trapped by the differential evaporation effect, as calculated in **Figure 1.10**. Therefore, the interplays among differential evaporation, thermocapillary convection, and Brownian motions can yield a very high enrichment factor.
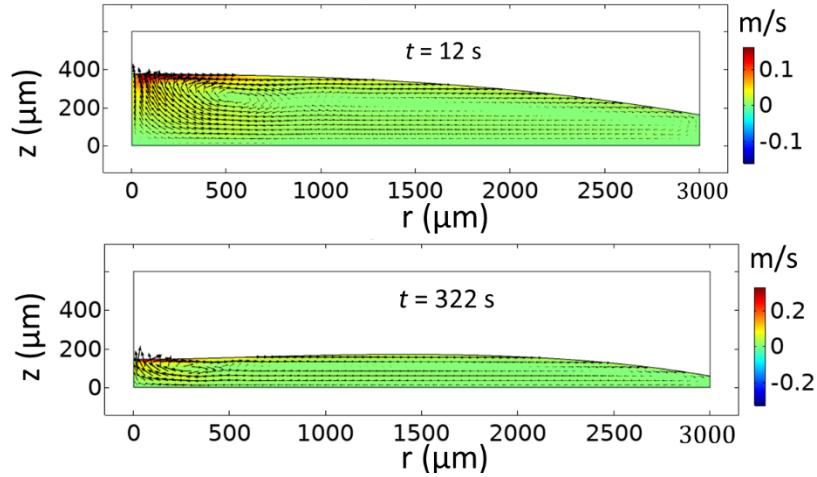
Figure 1.9 Velocity profile at t = 12 s and 322 s after the CO_2 laser focused to the center (r = 0 μm) position is turned on. The velocity profile shows the differential evaporation effect that terminates the liquid flow at the surface near the center position and the thermocapillary effect that creates a convection flow.
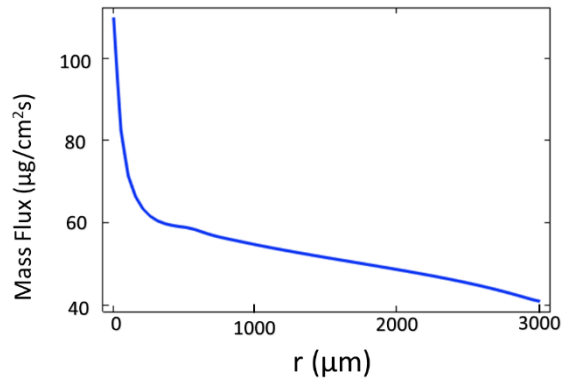
Figure 1.10 Mass Flux at water-air interface as a function of r at t = 322 s.

For a detailed model for enrichment of a particular type of particles such as DNA molecule, we need to take into account the specific properties of the particles[60] such as the Brownian (diffusion) force, drag force, gravity, and molecular interactions including Lennard-Jones, Coulombic and thermophoresis forces. These effects, together with the aforementioned

differential evaporation and thermocapillary effect that are universal to all particles in our experimental setup, will determine the details of the enrichment factor and particle behaviors.

1.4 Summary

In this chapter, a CO_2 laser-induced enrichment method was introduced that is applicable to numerous bioparticles regardless of their physical and chemical nature. Induced by evaporative mass-transport, the enrichment technique is capable of capturing particles over an extensive area and driving them to a single spot at the laser focus. It has been demonstrated that usingroughly 40 mW from a CO_2 laser, an enrichment factor as high as 100,000 can be achieved in 3-4 minutes. The temperature at the laser spot could be monitored and adjusted while maintaining an enrichment profile, such that temperature sensitive protocols can still be achieved. The ease and flexibility of IR-induced enrichment permits integration into a multitude of detection systems to support multi-dimensional biosensing and orthogonal tests for in-vitro diagnosis. The aggregation formation was demonstrated to show the capability of sample purification and quantification. Also, a microfluidic device to condition liquid samples using the differential diffusivity was demonstrated. The technique helps us achieve desired environments for testing of target particles from biofluids. The method is particularly suitable for removing/adding components to adjust the ionic strength and buffer condition for downstream analysis as ions usually have higher diffusivities than bio-makers of interest such as exosomes, extracellular vesicles, proteins and DNAs. Excellent agreement was found between the physical model and the experiment, making the results highly reliable and predictable. Thus, the method can be an effective means to measure the diffusivity of objects in the sample, which offers valuable insight for the physical properties of macromolecules such as their radius of hydration and geometry in different microenvironments.

1.5 References

1. C. D. Chin, V. Linder and S. K. Sia, *Lab Chip*, 2007, **7,** 41–57.

2. V. Linder, *The Analyst*, 2007, **132,** 1186.

3. B. Weigl, G. Domingo, P. LaBarre and J. Gerlach, *Lab on a Chip*, 2008, **8**, 1999.

4. M. A. Md Ali, K. (Ken) Ostrikov, F. A. Khalid, B. Y. Majlis and A. A. Kayani, *RSC Advances*, 2016, **6**, 113066–113094.

5. C. Zhang, K. Khoshmanesh, A. Mitchell and K. Kalantar-zadeh, *Analytical and Bioanalytical Chemistry*, 2010, **396**, 401–420.

6. H. C. Hamaker, *Physica*, 1937, **4**, 1058–1072.

7. W. B. Russel, *Annual Review of Fluid Mechanics*, 1981, **13**, 425–455.

8. D. A. Walker, C. E. Wilmer, B. Kowalczyk, K. J. M. Bishop and B. A. Grzybowski, *Nano Letters*, 2010, **10**, 2275–2280.

9. X. Xuan, J. Zhu and C. Church, *Microfluidics and Nanofluidics*, 2010, **9**, 1–16.

10. M. Tanyeri, M. Ranka, N. Sittipolkul and C. M. Schroeder, *Lab on a Chip*, 2011, **11**, 1786.

11. S. C. Hur, H. T. K. Tse and D. Di Carlo, *Lab Chip*, 2010, **10**, 274–280.

12. T. M. Squires and S. R. Quake, *Reviews of Modern Physics*, 2005, **77**, 977–1026.

13. H. Shafiee, J. L. Caldwell and R. V. Davalos, *Journal of the Association for Laboratory Automation*, 2010, **15**, 224–232.

14. S. Li, M. Li, K. Bougot-Robin, W. Cao, I. Yeung Yeung Chau, W. Li and W. Wen, *Biomicrofluidics*, 2013, **7**, 024106.

15. K. Klepárník and P. Boček, *BioEssays*, 2010, **32**, 218–226.I. Rodríguez-Villarreal, M. D. Tarn, L. A. Madden, J. B. Lutz, J. Greenman, J. Samitier and N. Pamme, *Lab Chip*, 2011, **11**, 1240–1248.

16. K. C. Neuman and A. Nagy, *Nature Methods*, 2008, **5**, 491–505.

17. L.-H. Yu and Y.-F. Chen, *Analytical Chemistry*, 2015, **87**, 2845–2851.

18. C. J. Wienken, P. Baaske, U. Rothbauer, D. Braun and S. Duhr, *Nature Communications*, 2010, **1**, 100.

19. S. Duhr, S. Arduini and D. Braun, *The European Physical Journal E*, 2004, **15**, 277–286.

20. H. Cong, J. Chen and H.-P. Ho, *Sensors and Actuators B: Chemical*, 2018, **264**, 224–233.

Chapter 2 Airjet-Induced Evaporative Fluid-Flow Manipulation in Paper-Based Microfluidic Devices

Microfluidic paper-based analytical devices (uPADs) have long been established as an attractive area for point-of-care testing (POCT) (27,28). These devices use paper as the key platform in the fabrication of various diagnostic assays. Paper, comprised primarily of cellulose fibers, presents an inexpensive and lightweight material which is beneficial for overall cost reduction. In addition, the presence of cellulose fibers allows the capability of wicking liquids via capillary action, thereby allowing simple operation without the use of external pumps(3). These advantages coupled with the biocompatibility and flexibility in diagnosing a variety of biomarkers has accelerated the growth of these devices as diagnostic tools.

Within this field, one of the most prominent readout methods for uPADs has been through colorimetric means(4,5). In colorimetric assays, detection of a biomarker is accompanied by a color change which is often proportional to the amount of biomarker present. Color change can be induced by various detection chemistries such as small-molecule organic indicators(6,7), metal nanoparticles(8–10), and chromogenic enzyme reactions(10–12). While the results can be either qualitative or quantitative, colorimetric assays represent a significant portion of current uPAD research due their user-friendly nature.

Despite the abundance of research in colorimetric detection, these assays suffer from key limitations which has inhibited commercial success. The frontmost of these issues remains in their poor sensitivity, having detection limits orders of magnitudes lower than those performed by clinical instruments(13). Sensitivity issues are often attributed to the inhomogeneous distribution of the colorimetric substance and the presence of background noise generated by either the paper or sample itself. In addition to poor sensitivity, lack of fluid control in

rudimentary uPADs has restricted their use to single reaction type assays(14). Fluid flow control and step-wise delivery of specific reagents is necessary if complex, multistep assays are to be achieved on paper.

Various methods to resolve these issues within colorimetric assays have been proposed. For sensitivity improvements, novel means of color generation and amplification have been the most widely studied alternative. Here, examples such as enzyme-nanoparticle conjugates(15), use of non-metallic nanoparticles(16–18), and enhanced metallic nanoparticle staining(19,20) act to further increase color development and subsequent contrast. Flow control on the other hand, has centered on reducing the sample flow rate through paper to achieve sequential delivery of multiple reagents. This has been accomplished using dissolvable solutes(21,22), creation of valves(23–25), and geometric adjustments(26,27). Fluid control can also contribute to improved sensitivity by increasing the interaction time between analyte and capture/reporter molecules. However, literature results for improving flow control and sensitivity remain somewhat exclusive issues as their end goal is either for integration into multistep assays or increasing the limit of detection, respectively.

In this chapter, a single airflow-based enrichment method that is capable of controlling the fluid flow and improving sensitivity for paper-based colorimetric assays. This method is accomplished by aiming an airflow nozzle perpendicular to a pre-wetted membrane. A differential evaporative gradient is induced as the area immediately underneath the airflow experiences a higher evaporation rate than the rest of the membrane. Due to the formation of this gradient, the surrounding liquid will migrate towards the spot in order to replenish the lost water. During this process, the replenishing water will carry any dissolved molecules towards this area such that they will be concentrated underneath the nozzle. While solute enrichment occurs while

the airflow source is stationary, fluid control and sequential delivery can be achieved by moving the nozzle in different positions across the filter surface.

We demonstrate the simplicity and flexibility of the airflow-enrichment method through its applications in colorimetric, paper-based protein and nucleic acid detection. Specifically, ELISA and isothermal RT-LAMP (Loop-mediated Amplification Process) assays were conducted as they show the most promise for being integrated into widespread POCT devices. In these assays, the colorimetric substance can be enriched via the airflow to reduce the homogenous distribution of color. After enrichment, formation of spot morphologies on the paper can be used to define the presence of analyte more accurately as compared to conventional means.

2.1 Theoretical basis for evaporative enrichment
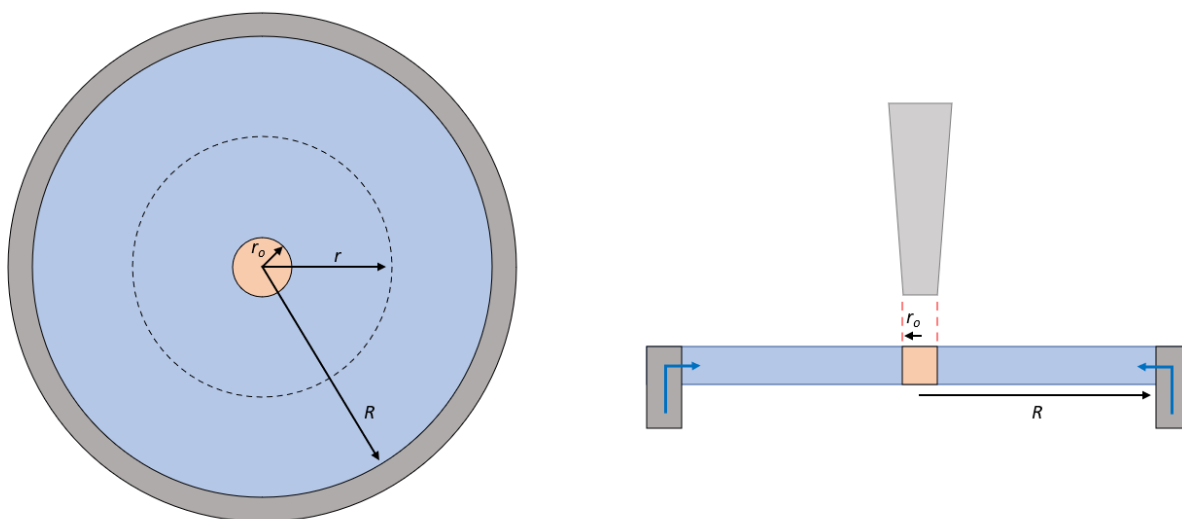
Figure 2.1 Schematic for the inward, radial replenishment of fluid and evaporation by ambient and airflow induced methods.

26

We define a system where a circular slice of porous media makes peripheral contact with an unlimited reservoir of fluid. At the perimeter of the porous slice, the capillary force induces the inward, radial penetration of liquid towards its center. At the center, a nozzle is positioned above the porous slice and generates a flow of air that is constrained within the nozzle radius. To model the system as a two-dimensional problem using planar coordinates, we assume that the thickness of the slice is much smaller than the radial dimensions.

During the enrichment process, two methods of evaporation occur on the wetted surface of the porous slice. The first is the ambient evaporation that is not affected by airflow, and the second is the airflow-induced evaporation. We therefore consider the total evaporation rate, K, which is the volume of evaporated liquid per area and time ($cm^3/m^2 \cdot s$) and is the sum of the ambient evaporation (K_o) and the airflow-induced evaporation (K_1):

$$K(r) = K_o + K_1 u(r_o - r) \qquad (2.1)$$

Where r_o is the radius of the airflow jet and u represents a unit step function when traveling away from r_o. Here, we assume that all evaporation will only occur on the top surface of the filter and that the airflow speed above the filter surface is negligible outside r_o.

When the steady state is reached and the enriched area under the nozzle has not completely dried, the definition of the derivative yields the following:

$$2\pi r K(r) dr = F(r - dr) - F(r)$$

$$2\pi r K(r) = -\frac{dF(r)}{dr} \qquad (2.2)$$

Where F refers to the volumetric flux of water per time (cm^3/s)

In order to drive the flux, Darcy's law for liquid flow can be expressed as:

$$\frac{F}{A} = -\frac{S}{\eta}\frac{dP}{dr} \quad (2.3)$$

Where the flux, F, of liquid flow is through a cylindrical surface having area $A = 2\pi rh$, S is the

permeability of the porous medium, η is the liquid viscosity, and P is the pressure of the liquid.

Substituting the cylindrical area into equation 3 and solving for the volumetric flux yields,

$$F = -\frac{2\pi h \gamma S}{\eta}r\frac{dP}{dr} \quad (2.4)$$

Substituting eq (4) into eq (2) and combining with eq (1),

$$2\pi r[K_o + K_1 u(r_o - r)] = \frac{2\pi h \gamma S}{\eta}\left[r\frac{d^2P}{dr^2} + \frac{dP}{dr}\right]$$

$$[K_o + K_1 u(r_o - r)] = \frac{h \gamma S}{\eta}\left[\frac{d^2P}{dr^2} + \frac{1}{r}\frac{dP}{dr}\right] \quad (2.5)$$

We define the boundary conditions as:

$$P(R) = P_c, \quad \frac{dP}{dr}\Big|_{r=0} = 0 \ (see \ Supplmentary \ for \ this \ BC)$$

$$P(r) = \frac{-\eta}{4h\gamma S}(K_o)(R^2 - r_o^2) - \frac{\eta}{4h\gamma S}(K_o + K_1)(r_o^2 - r^2) + P_c \quad 0 \le r \le r_o$$

$$P(r) = \frac{-\eta}{4h\gamma S}(K_o)(R^2 - r^2) + P_c \quad R \ge r \ge r_o \quad (2.6)$$

28

$$P(r) \geq 0. \, for \, all \, r. \quad When \, P(r) = 0 \, at \, a \, certain \, r, the \, region \, is \, dried \, up.$$

$$F(r_o) = -\frac{2\pi h\gamma S}{\eta} r \frac{dP}{dr}\Big|_{r_o} = \pi r_0{}^2 (K_o + K_1) \qquad (2.7)$$

We assume that when the wetted porous slice undergoes evaporation, it experiences varying degrees of water saturation. We therefore use the relation:

$$P(r) = P_c n(r) \qquad 0 \leq n(r) \leq 1. \quad (2.8)$$

where P_c is the capillary pressure, and n is the fraction of the pores (capillaries) that are completely saturated with water. The capillary pressure has the form:

$$P_c = \frac{2\sigma \cos\theta_S}{R_{eff}} \qquad (2.9)$$

Where σ is the surface tension, θ_s is the contact angle formed between solid and liquid, and, R_{eff} is the effective pore radius of the porous medium.

Integrating to find the water volume within r_o:

$$V(r_o) = 2\pi h\gamma \int_0^{r_o} n(r) r \, dr = \pi h\gamma r_o^2 - \frac{\pi \eta r_o^2}{8 P_c S} [K_o(2R^2 - r_o^2) + K_1 r_o^2] \qquad (2.10)$$

Taking the ratio between the water flux and volume determines the enrichment factor, a value which characterizes how effectively solutes are transported and concentrated under the airflow spot:

29

$$EF \text{ (enrichment factor)} = \frac{F(r_o)t}{V(r_o)} = \frac{(K_o + K_1)t}{h\gamma - \frac{\eta}{8P_cS}[K_o(2R^2 - r_o^2) - K_1 r_o^2]} \qquad (2.11)$$

In the case where the airflow-induced evaporation rate is much greater than the ambient evaporation rate over the entire wetted area ($K_1 r_o^2 \gg K_o R^2$), then (11) becomes

$$EF \text{ (enrichment factor)} = \frac{F(r_o)t}{V(r_o)} \sim \frac{K_1}{h\gamma + \frac{\eta}{8P_cS}K_1 r_o^2}t \qquad (2.12)$$

Therefore, in order to achieve a high enrichment within a given time period, the physical parameters of the porous slice and liquid should be considered. In addition, the parameters governed by the airflow (K_1, r_o) can also be controlled to further tune the enrichment factor. While r_o is a simple geometric parameter, K_1 is influenced by a variety of factors including airflow speed, humidity, temperature etc. These factors were incorporated into K_1 to simplify the model, however present additional areas to modify when looking to further increase the enrichment factor.

2.2 Overview of airflow-based enrichment on paper
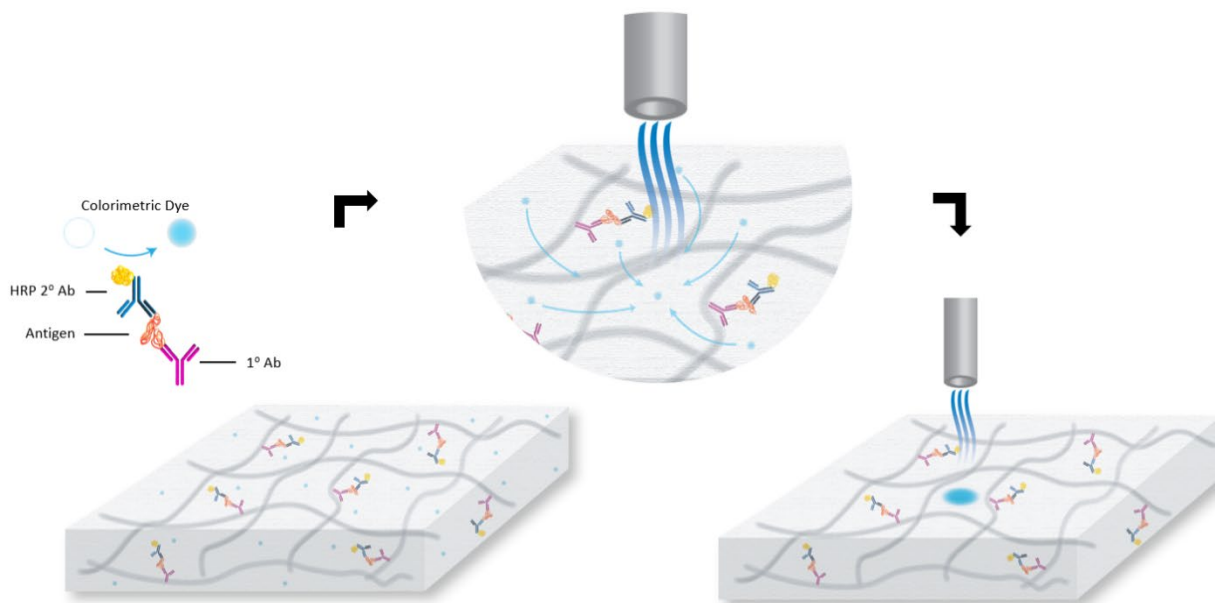
Figure 2.2 Schematic of the airflow-based enrichment for the concentration of colorimetric substrates produced during on-paper ELISA.

Figure 2.2 depicts the principle and setup for airflow-based enrichment in a paper matrix. This technique occurs on a pre-wetted filter that is suspended on a hollowed platform such that it is not contacting any surface underneath it. A nozzle connected to a nitrogen source is brought down perpendicular to the filter, and nitrogen is blown to create an evaporative gradient by reducing the thickness of a boundary layer containing saturated water vapor immediately above the surface(28,29). While any compressed air source can accomplish this, nitrogen was chosen as it is a "dry" (low humidity) source of airflow and gave consistent enrichment results when compared to compressed, ambient air. Due to displacement by the nitrogen airflow, the gradient is highest in the area immediately under the nozzle. Therefore, fluid flows driven by capillary action will converge towards this area from the filter's periphery to replenish the lost water. In doing so, any dissolved solutes will be carried by the flow and eventually accumulate underneath

the nozzle. We aim to use this technique to enhance the visibility and sensitivity of nucleic acid and protein colorimetric detection assays – including ELISA. For these assays, the colorimetric substance can be enriched to a single spot under the nozzle to improve the uniformity and concentration in addition to easier detection.

2.3 Static or dynamic movement of the airflow nozzle leads to solute enrichment and movement
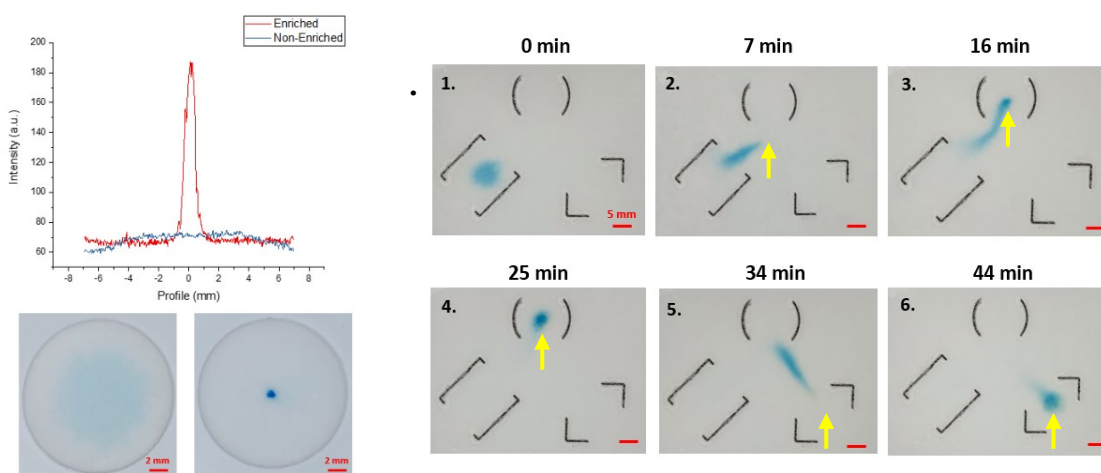
Figure 2.3 (a.) Profile plot of pixel intensity for enriched and non-enriched samples of dye deposited on paper. Images underneath represent corresponding non-enriched (before) and enriched (after) sample. **(b.)** Image sequence of dye localization in paper with hydrophobically patterned barriers indicated by black outlines. Images were taken during specified time points during dynamic movement of the nozzle. Actual nozzle position is indicated by the yellow arrow.

Airflow enrichment can accommodate two modes of fluid movement depending on whether the nozzle is in a static or dynamic position. When the nozzle position remains fixed **(Figure 2.3 (a))**, solute enrichment occurs as evaporative-loss leads to capillary-induced replenishment from the surrounding area. To visualize this effect, 7 uL of a blue, diluted dye solution was deposited on a 16mm diameter filter cutout. The cutout was placed concentric to a hollowed sample pad saturated with water, and a 200um diameter nozzle was aimed

perpendicular to the surface. Initiating the airflow establishes an evaporative gradient which generates fluid flows that are directed radially inward and transports the dye from a larger area to a defined spot. In addition to these flows along the 2D plane, any solutes will also move and localize at the paper's surface due to evaporation being a surface-driven phenomenon. As seen in the profile plot, this three-dimensional transport can thereby enhance visualization and detection of the initially diluted dye as it becomes more uniformly concentrated and unobscured from interacting with light.

Dynamic movement of the nozzle allows transportation of the solute to specified positions along the paper surface. The transport mechanism remains the same as the enrichment process, but the continual re-establishment of new evaporative gradients allows the direction of the replenishing flows to be controlled. In **Figure 2.3 (b).**, 1uL of blue dye was deposited on a wetted filter paper with hydrophobic patterns. The patterned filter paper was placed concentric to a sample pad saturated with water to prevent the paper from drying out. As less emphasis is placed on the degree of enrichment and more on the speed of transport, a wider 1.5 cm diameter nozzle accompanied with higher airflow speeds were used in comparison to that of the static enrichment. As shown in **Figure 2.3 (b).**, the localization of the dye can be controlled simply by changing the position of the nozzle above the paper surface.

2.4 Demonstration of sequential delivery using airflow-enrichment method
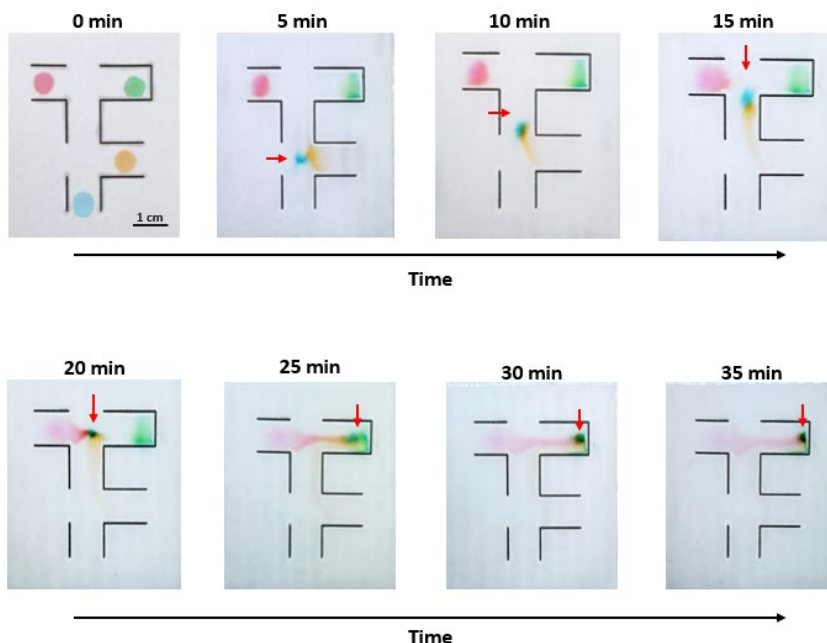
Figure 2.4 Image sequence for the sequential delivery of colored dyes by moving the airflow spot (red arrow) on a paper device patterned with PDMS channels. Black outlines represent the hydrophobic barriers and breaks in the outline indicate inlets to the channel design.

We demonstrate how controlled delivery of multiple reagents, visualized by different dye colors, can be accomplished using the airflow enrichment technique **(Figure 2.4)**. On a piece of filter paper patterned with hydrophobic channels, a combination of static and dynamic nozzle movements serves to mix and transport specified reagents, respectively. The filter paper is overlayed concentric to a hollow sample pad cutout, such that contact between the two materials was only made at the paper's perimeter. Then, 1uL of each dye color was spotted on the paper and could be mixed in a stepwise fashion based on the position of the nozzle - indicated by the red arrow. For this setup, water is transferred from the sample pad to the filter paper and eventually moves towards the interior of the channel through the openings in the design. While the openings act as inlets, the movement of the nozzle governs the position of the outlet and

34

determines where fluid flows will converge. As there is only one nozzle (outlet) in this system, additional openings were incorporated to reduce backflow and prevent early mixing of downstream reagents. For sections where the dye was to remain stationary throughout the process, such as the green dye, a closed channel was created by walling off three sides to create an area of dead volume.

The advantage of airflow-enrichment lies in the mechanism responsible for fluid control. For many designs focused on sequential delivery, the primary driving force for fluid transport is through capillary action(4,30). While capillarity is still present during airflow enrichment, it plays a secondary role with evaporation being the main driver of fluid movement. This has considerable effects when determining the overall design and costs of the assay. For one, conventional assays that rely on capillarity require relatively large sample volumes as they must continually imbue the device with the sample in order to reach the detection zone(31,32). For evaporative-driven transport, delivery of a small, initial volume of sample can be dragged to downstream detection zones simply by guiding it with the nozzle. In this case, the nozzle was able to transport 1uL of the initial blue dye from beginning to end. In addition, for assays that require interactions between molecules to occur, the airflow technique allows for more efficient mixing. Rather than relying of the slower process of diffusion, the nozzle can be left in a static position such as in the 20- and 35-minute time points **(Figure 2.4)** to facilitate the enrichment of different molecules and promote binding events. Finally, in designs that transport fluid through capillary action, the fluid flow is always "on" and specific obstructions are implemented in order to slow and control the flow rate for sequential delivery(22,30,31). For evaporative driven transport, the fluid flow can be turned "on" and "off" depending on whether any air is being

blown on the paper surface. The lack of any obstructions keeps the fabrication process simple

and reduces the amount of space needed to accommodate the obstruction itself.

2.5 Application in a multistep Immunoassay
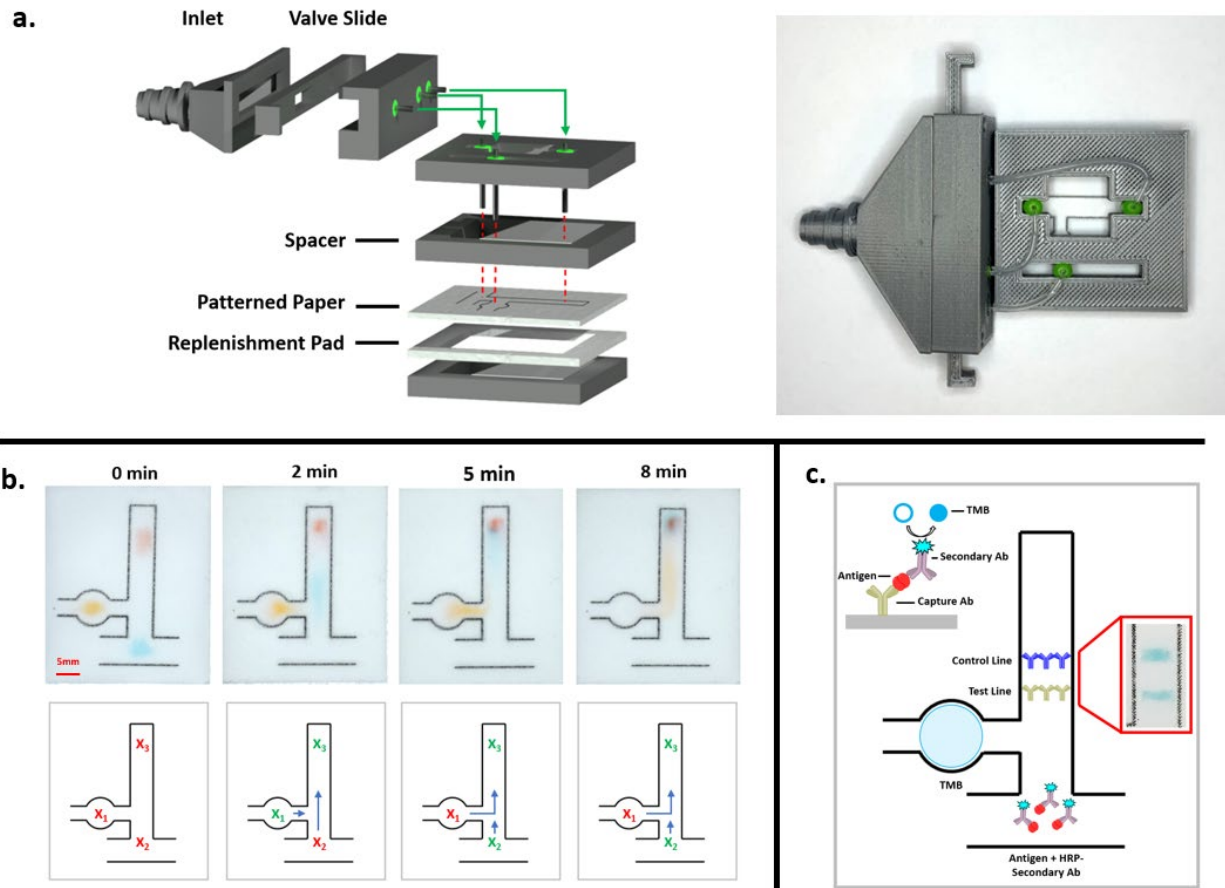
Figure 2.5 **(a.)** 3D-schematic of the POC device used for sequential delivery with the green arrows indicating tubing connections (left) and a top-down, real photo (right) of the assembled components. **(b.)** Demonstration of sequential delivery using dye as indicators. The top row shows the real photos taken at specified time points while the bottom row represents which nozzles are active (green) and inactive (red) as well as the strength of fluid flow from each channel (blue arrow). **(c.)** Schematic mapping the initial reagent spots for the multistep immunoassay. Red box is the real image of the test lines taken 32 minutes after starting the assay.

We next incorporate the airflow enrichment method in a possible POC device. In the previous figures, control of the fluid flow was dictated by the movement of a single nozzle and its relative position over the paper. As integrating a moving nozzle would be difficult in a POC device, we instead use a static arrangement of three individual nozzles (**Figure 2.5 (a)**) to accomplish step-wise delivery for an immunoassay. In addition, multiple nozzles were required as the dimensions of the patterned paper were reduced when compared in **Figure 2.3.** to decrease transport distances and consequently, the time for assay completion. Because of the constrained dimensions, a single nozzle cannot facilitate step-wise delivery as the evaporation would cause replenishing flows from multiple channels in the general vicinity. Therefore, for this setup, a single source of airflow originates from a central inlet and is then split up into the three separated nozzles - each of which the airflow can be turned on or off. The combination of active and inactive nozzles determines the predominant fluid flow within the patterned paper and therefore which reagent will be delivered faster.

A demonstration of stepwise delivery as visualized with dye is shown (**Figure 2.5 (b)**), where the delivery of the blue dye is achieved prior to that of the orange dye through a combination of active nozzles. Within this system, we define two means of fluid transport – one is the evaporative mass transport caused by the airflow nozzles, and the other is the replenishment transport driven by capillarity in maintaining a constant level of water saturation in the entire membrane. For an active nozzle far from the replenishment pad and walled off such as pos. 3, the fluid has reached the terminal position and will simply evaporate off and deposit any solutes in this location. However, for activated nozzles closer to the replenishment pad such as pos. 1 and 2., the evaporation will reduce the amount of fluid entering the channel and thereby slow the net movement of the fluid. This in turn will cause the delay of fluid to enter the main

channel and allow sequential delivery of reagents. Therefore, in **Figure 2.5b.**, the nozzles at X_1 and X_3 were first activated to delay movement of the orange dye such that the main replenishing flow was supplied by the blue channel. Once the blue dye reached the end, X_2 and X_3 were activated to allow the main source of replenishing flow from the orange dye.

The operation principle was then extended to an actual immunoassay, where 2uL of TMB, as well as 0.5uL of a pre-mixed solution of the antigen and the HRP-conjugated secondary antibody were deposited in separate channels (**Figure 2.5 (c)**). Test and control lines were immobilized downstream of these reagents prior to running in PBST buffer. During the assay, the antigen-secondary antibody complex was first drawn up the channel by activating nozzles 1,3 for 10 minutes. Not only does this step first transport the antigen complex to the detection lines, but also acts as a washing step for the latter duration to remove any unbound proteins in this area. Then, the nozzles at pos. 2,3 were activated to begin moving the TMB to the detection lines. Once a faint signal could be seen in the control line, the airflow was stopped, and time was given to allow further color development. The signal from these lines were clearly visible using 4nM of the antigen after running the airflow for roughly 25 minutes and allowing an additional 5 minutes for color development. Comparing the time scales for this immunoassay with the dye demonstration in **Figure 2.5 (b)**, the immunoassay takes much longer to complete. We believe the longer duration is primarily caused by two factors: (i) the relative low solubility of the unreacted TMB which leads to a higher retention factor on paper and requires more fluid to be evaporated to move it through the channel, (ii) the high salt concentration in the PBST running buffer which, after prolonged evaporation, will crystallize in the paper and act as a barrier for further fluid migration. Additional time is therefore spent re-dissolving these barriers when the activated nozzles switch position.

2.6 Improving visualization on paper for colorimetric RT-LAMP
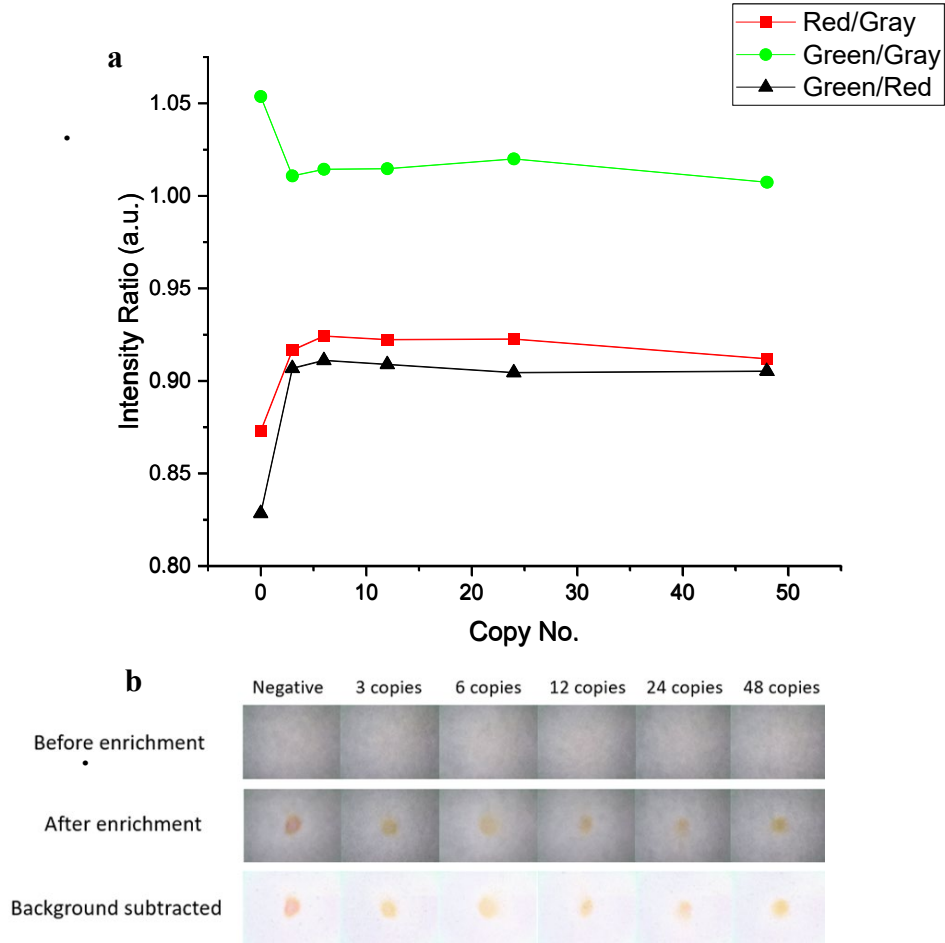
Figure 2.6 (a.) Plot of intensity ratio v. copy number between red and grayscale, green and grayscale, and green and red pixels. **(b.)** Before and after enrichment photos corresponding to different initial RNA copy numbers of the COVID-19 genome. Includes bottom "background subtracted" row to better visualize the color of each spot.

To test the whether the airflow enrichment could improve visualization in already established colorimetric assays, the technique was incorporated for on paper RT-LAMP in the detection of the COVID-19 genome (**Figure 2.6**). Heat inactivated viral particles were spiked in

nuclease-free water to the desired concentrations and then amplified using a commercially available RT-LAMP kit. For all copy numbers, amplification via LAMP was performed in test tubes for 60 minutes prior to depositing 3uL of the LAMP product onto paper strips. The strips were connected to a replenishing flow of nuclease-free water, and the airflow was turned on for 5 minutes before imaging. As shown in **Figure 2.6 (b)**, comparison between the "before" and "after" enrichment demonstrates how the process drastically improves the visibility of the dye. Furthermore, the enrichment did not alter the results of the test. The pH-sensitive color of the RT-LAMP result, either red (negative) or yellow (positive), is influenced by polymerase activity which releases a proton per each incorporated nucleotide. As the enrichment involves the concentration of molecules, we may expect false positives to occur due to co-enrichment of hydronium ions. However, a large shift in the green/red pixel intensity ratio from 0 (negative control) to 3 RNA copies supports the validity of the results as the negative control remains red. Due to the presence of buffer in the master mix solution, the final enrichment spot remains larger than previously demonstrated in **Figure 2.6 (a)** as early salt crystallization inhibits further condensation. While additives can be considered to reduce salt build up, we chose not to include any as it may affect the pH of the solution and therefore the accuracy of the test. Even with a larger spot size however, the results of the tests were still clear to the naked eye. The ease of integrating the airflow-based enrichment to various colorimetric assays, coupled with its short process time, demonstrates the flexibility and simplicity of the technique.

2.7 Improving on-paper ELISA sensitivity
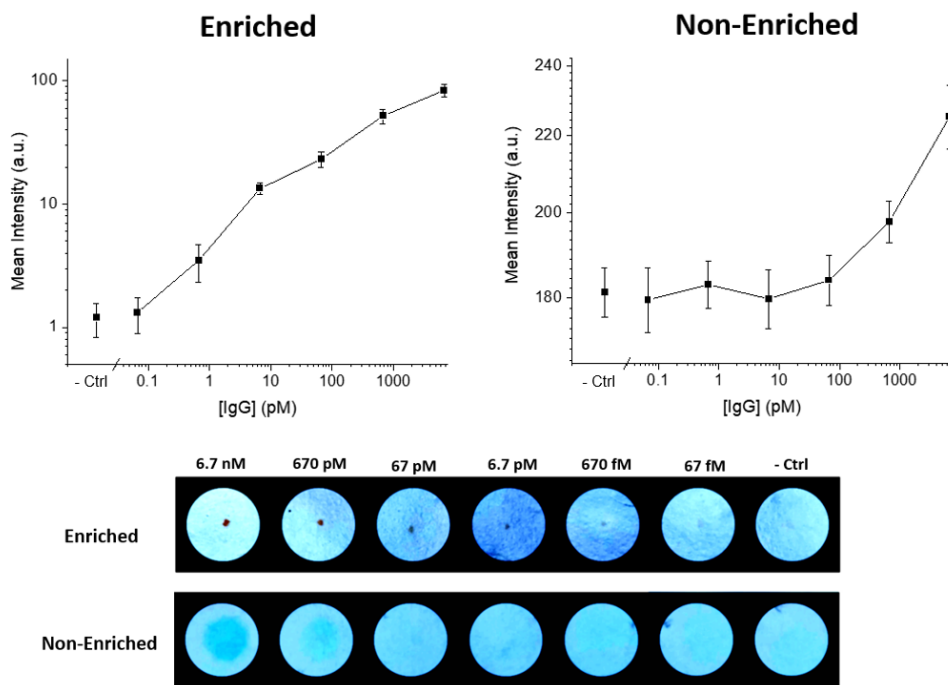
Figure 2.7: **(a.)** Comparison of Non-enriched and Enriched intensity plots for IgG concentrations from 67fM to 6.7nM. Error bars were calculated from three sets of experiments. **(b.)** Respective images from enriched and non-enriched samples from a single experimental set. Brightness and contrast were adjusted for better visualization of the TMB product.

We next use ELISA to model our enrichment method in improving the sensitivity for protein detection assays (**Figure 2.7**). While ELISA on paper has attracted multiple studies in the past, a key obstacle in detection is due to the non-uniformity and unequal distribution of the colored substrate(4,13). For this assay, TMB was chosen as the colorimetric substate as it has been shown to elicit one of the most sensitive responses in comparison with others. However, a drawback of using TMB lies in the relative insolubility of the oxidized product in water which is detrimental in the formation of an airflow-enriched spot. Therefore, the addition of the 0.1%

41

glycerol (v/v) in 2M HCl "stop" solution served multiple purposes. The first was to prevent further development of the substrate during enrichment and keep the colorimetric development times consistent between the enriched and non-enriched samples. The second was to protonate the TMB product to increase its solubility for enrichment. Glycerol was also added in small amounts to prevent early salt crystallization which halts spot formation during the evaporative process. The addition of an acidic solution to the TMB product causes a color change from blue to yellow which explains the different colors between the enriched and non-enriched samples. Despite the color change, the enriched samples were able to distinguish antigen concentrations by up to 2 orders of magnitude as compared to the non-enriched samples while only spending 15 minutes under airflow. This demonstrates the ease at which airflow enrichment can be integrated in current detection-based assays given the fraction of time needed to conduct the process and the much-improved detection sensitivity.

2. 8 Methodology

2.8.1 Colorimetric Assay Reagents

For the RT-LAMP assay, WarmStart Colorimetric RT-LAMP 2X Master Mix (DNA and RNA) were purchased New England Biolabs. The RT-LAMP primers against Nucleocapsid (N-1) and ORFla-1 genes were synthesized by Integrated DNA Technologies (IDT) and were designed according to a similar assay(33).The SARS-CoV-2 RNA (VR-3280SD) was purchased from American Type Culture Collection (ATCC) with an initial copy number of $3.4x10^5$ genome copies/ µL. For ELISA, Rabbit IgG, goat anti-rabbit IgG, TMB, Ultrapure water, 25% glutaraldehyde and chitosan were purchased from Millipore Sigma. Anti-rabbit IgG antibody conjugated with HRP was purchased from VectorLabs. The blocking buffer comprised of 0.05%

v/v Tween-20 and 1% w/v bovine serum albumin (BSA) in 1X phosphate-buffered saline (PBS). The antibody incubation solution consisted of the blocking buffer with the conjugated antibody at a 1:4000 ratio.

2.8.2 Enrichment Setup

Pre-pulled, 1mm O.D. capillaries were purchased from Tritech Research and the were tips sanded down to roughly 200um in diameter. A single tip was mounted on an xyz-stage through a 3D-printed holder and connected to a nitrogen source by rubber tubing. The mass flow rate was adjusted by pressure valves incorporated along the rubber tubing and specific values were determined by a mass flow meter purchased from Sierra Instruments. The specified sample was deposited on a cutout of Watman No. 1 filter paper and placed on a hollowed-out sample pad such that contact between the two materials only occurred at the perimeter of the filter cutout (FigureS1). This arrangement was then placed on a 3D-printed platform that also contained a hollow section and the capillary tip was brought about 2mm above the filter piece.

2.8.3 Enrichment of dye

The filter paper was punched into circular, 16 mm diameter cutouts and initially wetted with 10uL of DI water. After allowing the water to spread, 3uL of a diluted food dye solution was added to the center of the cutout which was then overlayed on top of a hollowed-conjugate pad saturated with DI water. The section was placed under the capillary tip and the nitrogen flow was turned on to a rate of 0.1 l/min. Airflow enrichment occurred for 15 minutes before imaging the section under a desktop ring-light using an iPhone 10 camera.

43

2.8.4 Fluid control

Patterns and outlines were designed using CAD software and printed directly on filter paper. The outlines were then traced over using a syringe containing a 10:1 ratio of PDMS to curing agent and subsequently placed in a 60°C oven to cure for 1 hour. Prior to enrichment, the patterened filter paper was dampened with DI water and 1uL of dye was spotted in the starting positions. The patterned filter paper was then placed on a replenishing pad and positioned 2mm under a 1.5 cm diameter metal nozzle with a nitrogen flow of 0.25 l/min. The relative position of the nozzle was changed by moving the platform with the filter paper.

2.8.5 Enrichment of RT-LAMP products on paper

Colorimetric LAMP was performed by adding 1 μL of the specified copy number of isolated SARS-CoV-2 RNA, 12.5 μL of the WarmStart Colorimetric RT-LAMP 2x Master Mix, 2.5 μL of the 10x primer mix and diluting with nuclease free water up to 25uL in total volume. All the solutions were prepared fresh and kept in closed test tubes to limit exposure to atmospheric CO_2. The reactions were then incubated in a 65°C oven for 60 min. The RT-LAMP samples were then taken out and placed on ice for 30 seconds before being stored at room temperature. For the enrichment, filter paper was cut into strips and 3uL each RT-LAMP product was deposited in the middle. Enrichment was carried out for 5 minutes with at 5uL/min replenishing flow of nuclease-free water from syringe pumps purchased from Harvard Apparatus. Before and after images were taken by a digital microscopic camera (AM7115MZT, Dino-Lite) with preset image capture settings.

2.8.6 RT-LAMP colorimetric readout signal analysis

The image signal analysis process of RT-LAMP colorimetric readout is shown in Figure S3. The effect of the GAMMA correction on the captured image is eliminated on the original image to remove the biased on the pixel intensity introduced by GAMMA correction [2]. The original image is subtracted by the background level first to remove the noise introduced from the background. A binary mask is generated through fixed intensity thresholding and preset enrichment spot size to determine the region of interest (ROI). The processed image is then convoluted with the binary mask to exclude pixels outside of the ROI. The convoluted color image is split into single color channels, and the average pixel intensity is calculated based on the average pixel intensity of the RGB color channel images. The image processing pipeline is developed based on ImageJ and MATLAB. All enrichment sample paper is processed using the same pipeline and parameter setting.

2.8.7 On-Paper ELISA

Double-sided tape was placed on a 3D-printed plate containing a 3 x 3 array of 12mm diameter holes (FigureS5). The tape was cut out around the holes and 16mm diameter filter circles were overlayed on top with only the perimeter making contact. Enhanced antibody immobilization was performed by adding 20uL of 0.25mg/mg chitosan (in 1% acetic acid) to all filter circles and letting them dry completely(34–36). After, 20uL of 2.5% glutaraldehyde in 1X PBS was added to the circles and the plate was covered with a petri dish for 1 hour to avoid evaporation. Each circle was then washed four times with 20uL of PBS with the excess liquid being removed between washes by pressing the plate against blotting paper. After washing, 10uL

of the capture antibody solution was deposited and allowed to incubate for 30 minutes. The circles were washed four times with 20uL of PBS and successively blocked with 30uL of blocking buffer for an additional 30 minutes. After blocking, the circles were washed once with 20uL of PBS and 3uL of the Rabbit IgG at specified concentrations was added to each circle. This was incubated for 15 minutes before adding 7 uL of the secondary antibody solution and incubating for another 2 minutes. The circles were then removed from the plate and into a wash bath containing 0.05% Tween in 1X PBS and a separator to prevent individual circles from contacting each other. The wash bath was placed on a shaker for 30 minutes with the wash solution being changed out every 10 minutes. The circles were then stored in 1X PBS until use.

2.8.8 Comparison between Enriched and Non-enriched Samples

For the non-enriched sample, the circles were removed from the PBS and transferred on blotting paper to remove excess liquid prior to being placed on a cleaned plate. The color development was initiated by adding 7 uL of TMB solution and allowing 80 seconds for the reaction to proceed before imaging under a desktop ring-light. A similar procedure was performed with the enriched samples except that the reaction time was shortened 70 seconds to include a washing step afterwards. This step consisted of transferring the circle onto blotting paper and depositing 1 mL of ultrapure water to reduce salt levels. Then, 6 uL of 0.1% glycerol (v/v) in 2M HCl was added to the circle to stop the reaction during the enrichment process. The circle was enriched under the 200um diameter capillary nozzle for 15 minutes until completely dry and imaged under the ring-light.

2.8.9 ELISA Imaging

The images were processed through ImageJ by first subtracting the background by 50 pixels, then enhancing the contrast by 0.3%. The images were then split into RGB color channels and inverted. For the non-enriched samples, the selected ROI consisted of the entire filter circle diameter. In the enriched samples, a binary mask was used to highlight the enriched area and the ROI consisted of a 2mm diameter section around the highlight. After finding the mean respective mean intensities from each channel, the magnitude of the combined channels was calculated for the mean intensity.

2.9 Summary

To summarize, we present a simple, airflow-based method that can manipulate fluid flows in paper matrices. Depending on how the method is used, enrichment or lateral transportation of solutes can be performed using minimal external equipment. The enrichment process was integrated into existing colorimetric assays for genomic and proteomic detection to significantly enhance the visualization and sensitivity of the assays. While the enrichment aspect was explored in depth for this study, we also demonstrate how multistep, sequential delivery of reagents can be accomplished for future assays requiring higher complexity. This method ultimately presents a unique example where sensitivity improvement and fluid control can be accomplished using a single technique. Despite focusing on colorimetric detection assays in this study, we envision that this method can be easily incorporated into the broader field of mPADs.

This chapter is based on the following paper: Edward Wang, Zhilin Guo, Rui Tang and Yu-Hwa Lo, Using airflow-driven, evaporative gradients to improve sensitivity and fluid control in colorimetric paper-based assays.

2.10 References

1.   Lisowski P, Zarzycki PK., Microfluidic paper-based analytical devices (μPADs) and micro total analysis systems (μTAS): Development, applications and future trends, *Chromatographia*, 2013, **76**, 1201–14.

2.   Whitesides GM., The origins and the future of microfluidics. *Nature*, 2006, **442**, 368–73.

3.   Yetisen AK, Akram MS, Lowe CR., Paper-based microfluidic point-of-care diagnostic devices, *Lab on a Chip*, 2013, **13**, 2210–51

4.   Akyazi T, Basabe-Desmonts L, Benito-Lopez F., Review on microfluidic paper-based analytical devices towards commercialization, *Analytica Chimica Acta*, 2018, **1001**, 1–17.

5.   Nery EW, Kubota LT., Sensing approaches on paper-based devices: A review, *Analytical and Bioanalytical Chemistry*, 2013, **405**, 7573–95.

6.   Abe K, Suzuki K, Citterio D., Inkjet-printed microfluidic multianalyte chemical sensing paper, *Analytical Chemistry*, 2008, **80**, 6928–34.

7.   Martinez AW, Phillips ST, Butte MJ, Whitesides GM., Patterned paper as a platform for inexpensive, low-volume, portable bioassays, *Angewandte Chemie - International Edition*, 2007, **46**, 1318–20

8.   Ornatska M, Sharpe E, Andreescu D, Andreescu S., Paper bioassay based on ceria nanoparticles as colorimetric probes, *Analytical Chemistry*,2011, **83**, 4273–80.

9.   Choleva TG, Kappi FA, Giokas DL, Vlessidis AG., Paper-based assay of antioxidant activity using analyte-mediated on-paper nucleation of gold nanoparticles as colorimetric probes. *Analytica Chimica Acta*, 2015, **860**, 61–9

10.   Teengam P, Siangproh W, Tuantranont A, Vilaivan T, Chailapakul O, Henry CS., Multiplex Paper-Based Colorimetric DNA Sensor Using Pyrrolidinyl Peptide Nucleic

Acid-Induced AgNPs Aggregation for Detecting MERS-CoV, MTB, and HPV Oligonucleotides. *Analytical Chemistry*, **89**, 5428–35

11.   Chen W, Fang X, Li H, Cao H, Kong J., A Simple Paper-Based Colorimetric Device for Rapid Mercury(II) Assay, *Scientific Reports*, 2016, **6**,1–7

12.   Wang X, Li F, Cai Z, Liu K, Li J, Zhang B, et al., Sensitive colorimetric assay for uric acid and glucose detection based on multilayer-modified paper with smartphone as signal readout. *Analytical and Bioanalytical Chemistry*, 2018, **410**, 2647–55.

13.   Hu J, Wang SQ, Wang L, Li F, Pingguan-Murphy B, Lu TJ, et al., Advances in paper-based point-of-care diagnostics. *Biosensors and Bioelectronics*, 2014, **54**, 585–97.

14.   Parolo C, de la Escosura-Muñiz A, Merkoçi A., Enhanced lateral flow immunoassay using gold nanoparticles loaded with enzymes. *Biosensors and Bioelectronics*, 2013, **40**, 412–6.

15.   Sakurai A, Takayama K, Nomura N, Yamamoto N, Sakoda Y, Kobayashi Y, et al. Multi-colored immunochromatography using nanobeads for rapid and sensitive typing of seasonal influenza viruses. *Journal of Virological Methods*, 2014, **209**, 62–8.

16.   Yao L, Teng J, Zhu M, Zheng L, Zhong Y, Liu G, et al., MWCNTs based high sensitive lateral flow strip biosensor for rapid determination of aqueous mercury ions, *Biosensors and Bioelectronics*, 2016, **85**, 31–6.

17.   Shirshahi V, Tabatabaei SN, Hatamie S, Saber R., Functionalized reduced graphene oxide as a lateral flow immuneassay label for one-step detection of Escherichia coli O157:H7, *Journal of Pharmaceutical and Biomedical Analysis*, 2019, **164**, 104–11.

18.   Kim W, Lee S, Jeon S., Enhanced sensitivity of lateral flow immunoassays by using water-soluble nanofibers and silver-enhancement reactions, *Sensors and Actuators, B: Chemical*, 2018, **273**, 1323–7.

19. Rodríguez MO, Covián LB, García AC, Blanco-López MC., Silver and gold enhancement methods for lateral flow immunoassays. *Talanta*, 2016, **148**, 272–8.

20. Kasetsirikul S, Shiddiky MJA, Nguyen NT., Challenges and perspectives in the development of paper-based lateral flow assays, *Microfluidics and Nanofluidics*, 2020, **24**,17

21. Kim TH, Hahn YK, Kim MS., Recent Advances of Fluid Manipulation Technologies in Microfluidic Paper-Based Analytical Devices (µPADs) toward Multi-Step Assays, *Micromachines*, 2020, **11**, 269

22. Jahanshahi-Anbuhi S, Henry A, Leung V, Sicard C, Pennings K, Pelton R, et al., Paper-based microfluidics with an erodible polymeric bridge giving controlled release and timed flow shutoff, *Lab on a Chip*, 2014, **14**, 229–36

23. Lutz B, Liang T, Fu E, Ramachandran S, Kauffman P, Yager P., Dissolvable fluidic time delays for programming multi-step assays in instrument-free paper diagnostics, *Lab on a Chip*, 2013, **13**, 2840–7

24. Lafleur LK, Bishop JD, Heiniger EK, Gallagher RP, Wheeler MD, Kauffman P, et al., A rapid, instrument-free, sample-to-result nucleic acid amplification test, *Lab on a Chip*, 2016, **16**, 3777–87

25. Koo CKW, He F, Nugen SR., An inkjet-printed electrowetting valve for paper-fluidic sensors, *Analyst*, 2013, **138**, 4998–5004

26. Li X, Tian J, Shen W., Progress in patterned paper sizing for fabrication of paper-based microfluidic sensors, *Cellulose*, 2010, **17**, 649–59

27. Park J, Shin JH, Park J-K., Pressed Paper-Based Dipstick for Detection of Foodborne Pathogens with Multistep Reactions, *Analytical Chemistry*, 2016, *88*, 3781-3788

28.   Preechakasedkit P, Siangproh W, Khongchareonporn N, Ngamrojanavanich N, Chailapakul O., Development of an automated wax-printed paper-based lateral flow device for alpha-fetoprotein enzyme-linked immunosorbent assay, *Biosensors and Bioelectronics*, 2018, **102**, 27–32.

29.   Fu E, Lutz B, Kauffman P, Yager P., Controlled reagent transport in disposable 2D paper networks., *Lab on a Chip*, 2010, **10**, 918–20

30.   Kim TH, Hahn YK, Lee J, Noort D van, Kim MS., Solenoid Driven Pressure Valve System: Toward Versatile Fluidic Control in Paper Microfluidics, *Analytical Chemistry* 2018, **90**, 2534–41

31.   J. Toley B, A. Wang J, Mayuri Gupta, R. Buser J, K. Lafleur L, R. Lutz B, et al., A versatile valving toolkit for automating fluidic operations in paper microfluidic devices. *Lab on a Chip*, 2015, **15**, 1432–44

32.   Fratzl M, Chang BS, Oyola-Reynoso S, Blaire G, Delshadi S, Devillers T, et al. Magnetic Two-Way Valves for Paper-Based Capillary-Driven Microfluidic Devices, *ACS Omega*, 2018, **3**, 2049–57

33.   Verma MS, Tsaloglou MN, Sisley T, Christodouleas D, Chen A, Milette J, et al., Sliding-strip microfluidic device enables ELISA on paper, *Biosensors and Bioelectronics*, 2018, **99**, 77–84.

34.   Ho Shin J, Park J-K., Functional Packaging of Lateral Flow Strip Allows Simple Delivery of Multiple Reagents for Multistep Assays, *Analytical Chemistry*, 2016, **88**, 10374–10378

35.   Li B, Yu L, Qi J, Fu L, Zhang P, Chen L., Controlling Capillary-Driven Fluid Transport in Paper-Based Microfluidic Devices Using a Movable Valve, *Analytical Chemistry*, 2017, **89**, 5707–12.

36.   Liu M, Wu J, Gan Y, Hanaor DAH, Chen CQ., Tuning capillary penetration in porous media: Combining geometrical and evaporation effects, *International Journal of Heat and Mass Transfer*, 2018, **123**, 239-250.

37.   Liu Z, Hu J, Zhao Y, Qu Z, Xu F., Experimental and numerical studies on liquid wicking into filter papers for paper-based diagnostics, *Applied Thermal Engineering*, 2015, **88**, 280–7

38.   Liu M, Wu J, Gan Y, Hanaor DAH, Chen CQ., Evaporation Limited Radial Capillary Penetration in Porous Media, *Langmuir*, 2016, **32**, 9899–904

39.   Conrath M, Fries N, Zhang M, Dreyer ME, Conrath M, Fries N, et al., Radial Capillary Transport from an Infinite Reservoir, *Transp Porous Med*, 2010, **84**, 109–32.

40.   Madhu NT, E RP, Pradeep A, Satheesh Babu TG., Design and simulation of fluid flow in paper based microfluidic platforms, *IOP Conf. Ser.: Mater. Sci. Eng.*, 2019, **577**, 012104

41.   Patari S, Mahapatra PS., Liquid wicking in a paper strip: An experimental and numerical study., *ACS Omega*, 2020, **5**, 22931–22939

42.   Neriah A, Assouline S, Shavit U, Weisbrod N., Impact of ambient conditions on evaporation from porous media, *Water Resources Research*, 2014, 50, 6696–712

43.   Deegan RD, Bakajin O, Dupont TF, Huber G, Nagel SR, Witten TA., Contact line deposits in an evaporating drop. *Phys. Rev. E*, 2000, **62**, 756

44.   Mosthaf, K., R. Helmig, D. Or, Modeling and analysis of evaporation processes from porous media on the rev scale, *Water Resour. Res.*, 2014, **50**, 1059– 1079

45.   Haghighi, E., E. Shahraeeni, P. Lehmann, D. Or, Evaporation rates across a convective air boundary layer are dominated by diffusion, *Water Resour. Res.*, 2013, **49**, 1602– 1610

46. Modha S, Castro C, Tsutsui H., Recent developments in flow modeling and fluid control for paper-based microfluidic biosensors, *Biosensors and Bioelectronics*, 2021, **178**, 113026

47. Shin JH, Park J, Kim SH, Park JK., Programmed sample delivery on a pressurized paper. *Biomicrofluidics*, 2014, **8**, 54121.

48. Rivas L, Medina-Sánchez M., de La Escosura-Muñiz A, Merkoçi A., Improving sensitivity of gold nanoparticle-based lateral flow assays by using wax-printed pillars as delay barriers of microfluidics, *Lab on a Chip* 2014, **14**, 4406–14

49. Zhang, Y.; Odiwuor, N.; Xiong, J.; Sun, L.; Nayaruaba, R. O.; Wei, H.; Tanner, N., Rapid molecular detection of SARS-CoV-2 (COVID-19) virus RNA using colorimeteric LAMP., *medRxiv*, 2020, 2020.02.26.20028373

50. Wang S, Ge L, Song X, Yu J, Ge S, Huang J, et al., Paper-based chemiluminescence ELISA: Lab-on-paper based on chitosan modified paper device and wax-screen-printing, *Biosensors and Bioelectronics*, 2012, **31**, 212–8.

51. Chan SK, Lim TS., A straw-housed paper-based colorimetric antibody-antigen sensor. *Analytical Methods*, 2016, **8**, 1431–6

52. Ma L, Nilghaz A, Choi JR, Liu X, Lu X., Rapid detection of clenbuterol in milk using microfluidic paper-based ELISA, *Food Chemistry*, 2018, **246**, 437–41.

Chapter 3 Airjet-Induced Reversal of the Coffee-Ring Effect for Liquid Phase Sample Preparation

Introduction

The sensitivity in detecting biological analytes is determined by the upstream sample preparation steps [1,2], in addition to the recognition and signal transduction mechanisms that follow. Regarding nucleic acid biosensors, significant advancements in detection have been reported[3,4], yet progress in sample enrichment and pre-treatment have been slower. Currently, the use of magnetic beads has been a popular tool for sample preparation in many biological applications, including nucleic acid extraction and purification[5,6]. However, a major challenge with this method is the loss of analyte that occurs during the multiple washing and transfer steps – often having an analyte extraction efficiency under 1%. This extraction inefficiency manifests the sensitivity bottleneck in current biosensors for *in-vitro* diagnosis. Therefore, it is essential to develop a sample processing method which can effectively concentrate the majority of analytes within a minimal volume of 1-2uL. In addition, a method which removes extraneous solutes that may interfere with downstream analysis could be integrated into the workflow of various biosensors, regardless of the amplification and signal readout mechanisms.

Several sample preconcentration techniques have been developed based on solid-phase affinity [7,8], liquid-phase affinity [9,10], and electrophoresis [11–13]. However, these methods are limited in scope as they heavily depend on the analyte's charge, surface binding affinity, or solvent miscibility. A preconcentration method which functions independently of an analyte's properties is through solvent removal by evaporation [14,15]. As many analytes are either dissolved or suspended in a solvent, the volume reduction caused by evaporation serves as a concentrative step. While isotropic evaporation in general leads to analyte concentration,

54

multiple studies have further improved the degree of enrichment by utilizing the intrinsic hydrodynamic flows that occur during evaporation. The most common of which, is derived from the coffee-ring effect (CRE) in a drying sessile droplet [16].

The CRE is a common phenomenon in drying droplets which is characterized by the formation of a ring-like deposit [17,18]. This pattern is driven by a differential evaporative gradient, which is highest at the perimeter of the droplet. Here, the large evaporative flux induces a radially outward flow as fluid from the droplet interior moves towards the periphery to replenish the lost fluid. As a result, any dissolved solutes or suspended particles are carried to the contact line and deposited [19]. The CRE therefore represents a passive method in which particles can further be localized during evaporation, rather than remaining equally distributed [20].

Due to the nature of droplets and their prevalence in a variety of different applications, the CRE is viewed as beneficial for specific situations but mostly detrimental concerning analyte extraction and transfer for *in-vitro* diagnosis [21]. Therefore, while multiple studies have taken advantage of the CRE to concentrate chemical and biological analytes for detection [22,23], separation [24,25], and patterning [26–28], most research efforts have been focused on suppression of the CRE [29]. During CRE suppression, the analytes can either be uniformly deposited over the area of the original droplet or reversed such that the particles are concentrated at a single spot in the center. CRE reversal can be achieved through electroosmosis [30], electrowetting [26,31], surface wave acoustics [32,33], or infrared laser heating [34]. In addition, microfabricated surface patterning can be used to create a superhydrophobic surface which prevents droplet pinning that is necessary for CRE development [35,36]. While the above methods have been shown to reverse CRE, the process and setup are complicated and depend on

55

the properties of the particles, including size and charge. Above all, with or without CRE, any evaporation method enriches not only the analytes but also the other solutes in the buffer such as salt which can disrupt downstream analysis.

In this chapter, we present an airjet-induced method to enrich analytes in a liquid sample by reversing the coffee-ring flow. The method is capable of driving analytes from a relatively large sample volume towards a small region under the airjet – allowing easier and efficient transfer to downstream analysis. The method has a simple setup, consisting of a compressed air source, an air heater, and the airjet nozzle. In addition, a small amount of surfactant (e.g. methyl cellulose) is mixed with the sample to suppress fluid turbulence. Coffee-ring flow reversal is achieved by aiming the nozzle perpendicular to the liquid surface and initiating the airjet to increase local evaporation. The localized increase in evaporative flux establishes a differential evaporative gradient and induces fluid flows towards the area to replenish the lost liquid. During this process, dissolved molecules or suspended particles are carried by the flow and become highly concentrated in a minuscule area underneath the nozzle.

We demonstrate the design by concentrating a range of particles and biological analytes – specifically nucleic acids. Spiked samples containing λ-DNA, HeLa-S3 RNA, and heat inactivated SARS-CoV-2 were used as model analytes and reduction of the cycle threshold value (C_q) in PCR analysis was used to quantify analyte enrichment and collection efficiency. To minimize potential adverse effects on downstream reactions (e.g. PCR) due to co-concentration of salt and other non-volatile components in the sample, polyethylene glycol (PEG) was mixed with the sample as co-enrichment of PEG forms a matrix under the airjet to reduce salt accumulation. The airjet enrichment method was employed in both microfluidic and mesofluidic systems to handle sample volumes from <100uL to >1mL to cover the sample volumes used in

common laboratory practices concerning PCR-based detection. The goal of this approach is to address the bottleneck in sample preparation by significantly increasing the analyte collection efficiency, up to 100 times more than current practices. This increase in efficiency can improve the sensitivity and repeatability of biosensing and in-vitro diagnosis.

3.1 Using an Airjet to Reverse the Coffee-Ring-Effect (CRE)
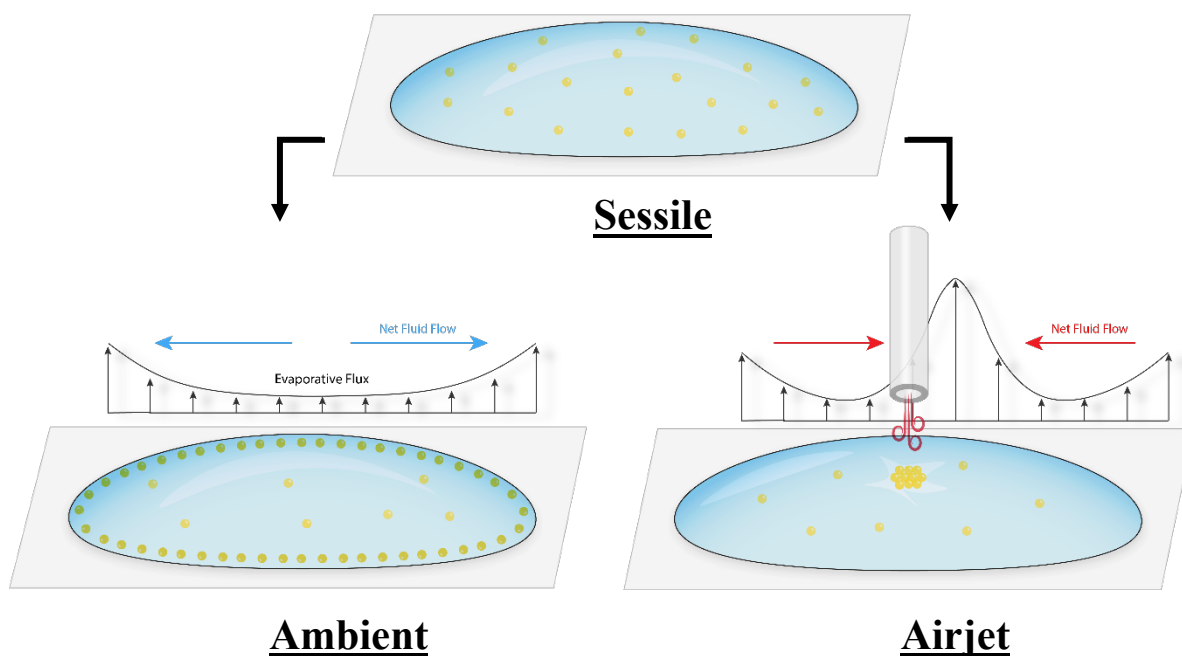
Figure 3.1. Schematic of airjet enrichment to reverse coffee-ring flows and the comparison of the resulting deposition patterns with that of ambient evaporation.

The operating principle for airjet enrichment is depicted in **Figure 3.1**, which illustrates the particle distribution under ambient evaporation and airjet enrichment in a sessile droplet. The development of the CRE has been attributed to the non-uniform evaporative profile across the droplet's surface. For ambient evaporation, the evaporative flux is greatest at the contact line, due to the relatively larger proportion of the liquid-air interface [37]. As a result, an evaporative gradient is established at the droplet periphery, and a radially outward flow is formed from the

interior to replenish the lost fluid. This flow carries any solutes or suspended particles towards the contact line and results in the familiar ring-like pattern.

Airjet enrichment reverses this radial flow by establishing a large evaporative flux at the center of the droplet. This is achieved by positioning a nozzle above the droplet and directing a jet of air perpendicular to its surface. The airjet displaces the boundary layer comprised of saturated water vapor which lies directly above the liquid-air interface. Displacement of the boundary layer leads to enhanced diffusion across the interface [18,38] and shifts the evaporative gradient towards the area under the airjet. In addition, as the speed of enrichment is heavily dependent on the evaporation rate, the temperature of the airjet can be used to control the overall evaporation rate.

3.2 Suppression of Airjet-Induced Turbulence
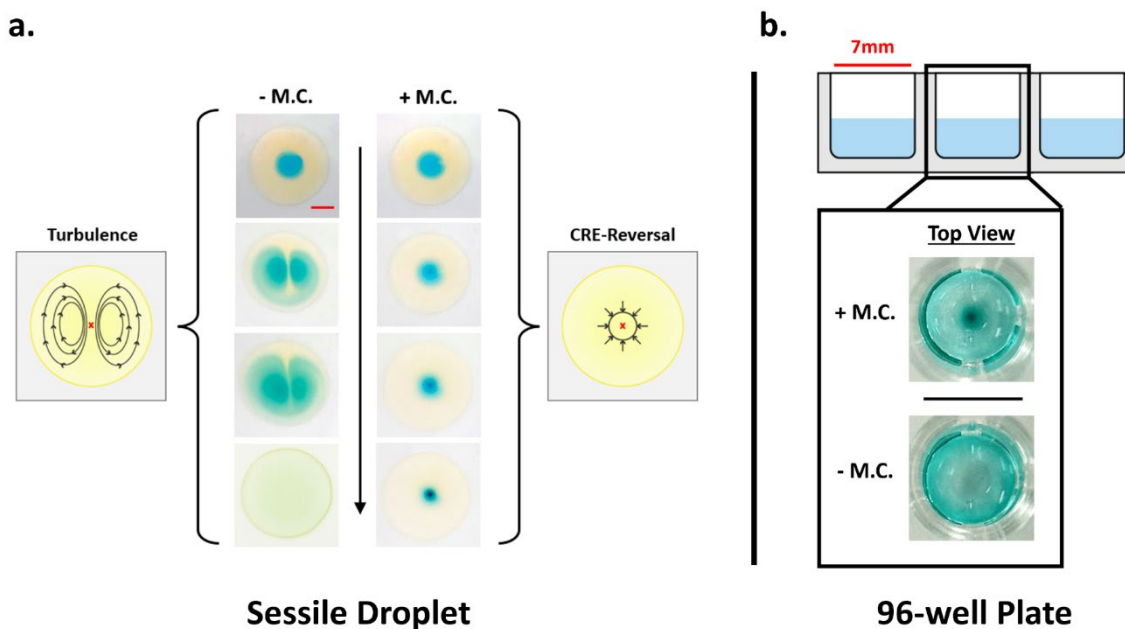
Figure 3.2 (a) Images of fluid behavior under an airjet in the absence (- M.C.) and presence (+ M.C.) of the methyl cellulose surfactant in a droplet as the process progresses (from top to bottom). Scale bar: 4mm. **(b)** Images from a 96-well plate after enrichment with (+ M.C.) and without (- M.C.) methyl cellulose.

The desirable airjet enrichment effect is obtained by the introduction of an additive to "stabilize" the surface and suppress streaming and turbulence. The airjet inevitably imparts shear forces on the liquid surface, which causes turbulent motion in the fluid and disrupts the radial flow driven by evaporation. The additive used in this study is methyl cellulose, a relatively inert and biocompatible component acting as both a surfactant and a mild thickening agent. **Figure 3.2 (a)** demonstrates how the presence of methyl cellulose mitigates the airjet-induced secondary flows, in order to achieve a condensed spot through CRE-reversal. In a 20uL sessile droplet which has been dyed yellow, a region of blue dye was added to visualize liquid movement. In the absence of methyl cellulose, turbulent, vortical flow patterns quickly develop within the droplet

upon initiating the airjet. This leads to increased mixing between the blue and yellow dye such that a uniformly green solution eventually forms. However, by adding methyl cellulose to the droplet, the turbulent patterns are suppressed and evaporative-driven, radial flow dominates as indicated by the increasingly concentrated blue region of dye.

Similar behavior was also observed for fluid contained in a 96-well plate (**Figure 3.2 (b)**). In individual wells, 100uL of a blue dye solution was deposited and allowed to evaporate underneath the airjet. For solutions containing methyl cellulose, a clear enrichment spot of concentrated dye was formed, while solutions lacking methyl cellulose had the dye evenly distributed throughout the entire process. The presence of methyl cellulose is therefore critical to the enrichment process, and its addition allows enrichment to occur in various fluid containers. The mechanism in which methyl cellulose can suppress the airjet-induced fluid flows is attributed to its surfactant properties. Surfactants have been shown to reduce wave activity in liquids through the Gibbs-Marangoni effect [39]. Here, the formation of capillary waves is attenuated as they would produce localized variations in surfactant density at the liquid-air interface, and consequently lead to counteracting surface-tension gradients. However, not all surfactants screened during this study could completely inhibit the airjet-induced turbulence to the same degree as methyl cellulose. Therefore, additional properties are likely to play a role in the effectiveness of surface stabilization. While this study focuses on enrichment in aqueous solutions, we have also successfully performed enrichment on volatile organic solvents such as ethanol using PDMS as the surfactant (supplementary: Ethanol). Continued exploration of surfactants and their effects on a variety of solvents will therefore yield more insight into the optimal properties required for airjet enrichment.

3.3 Ubiquitous Enrichment
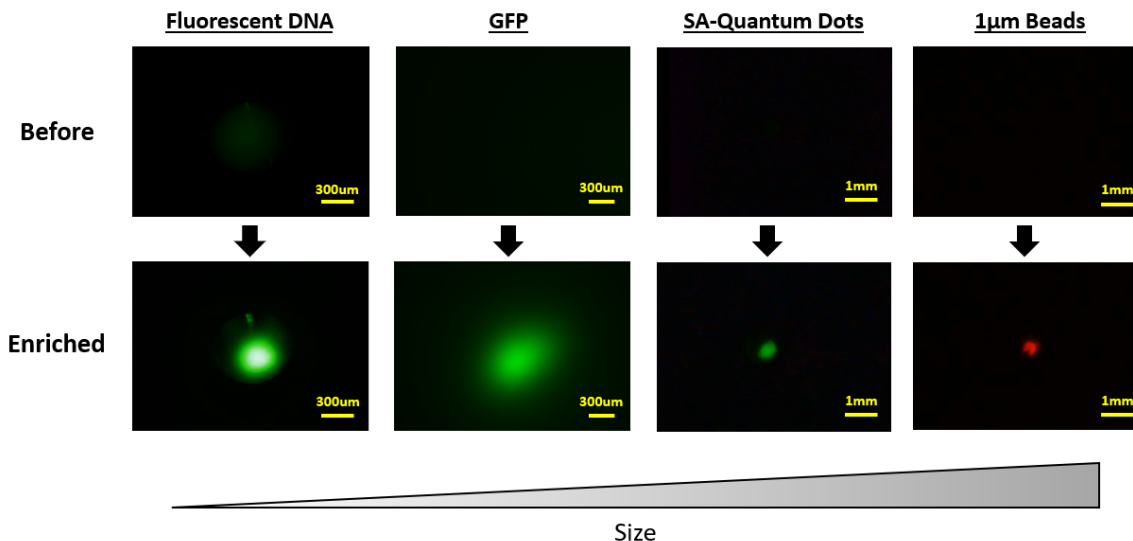
Figure 3.3 Images before and after enrichment with equal exposure time for FITC-tagged DNA oligonucleotides, green fluorescent protein (GFP), streptavidin-functionalized quantum dots, and 1um fluorescent beads

Airjet enrichment can effectively improve detection sensitivity and concentrate various fluorescent biomacromolecules and particles, regardless of their size of size as shown in **Figure 3.3**. Solutions containing FITC-tagged DNA oligonucleotides, green fluorescent protein (GFP), streptavidin-functionalized quantum dots, and 1um fluorescent beads were deposited on a hydrophilic glass slide. Methyl cellulose was then added to the droplet to prevent fluid turbulence caused by airflow. A glass pipette with a 1.5mm I.D. exit nozzle was then used to create an airjet, which was connected to a nitrogen tank and controlled by a digital mass flow meter. For each solution, the fluorophores could be concentrated to a defined spot underneath the airjet measuring 300-500um in diameter. As a result, fluorescence intensity was greatly increased within this spot, which can be beneficial for either visual detection or collection and transfer purposes in dilute solutions. In addition, the enrichment process did not seem to have any

adverse effects on the respective fluorophores, including GFP, which requires proper protein folding to exhibit fluorescence. Therefore, successful enrichment in these tests demonstrates the broad applicability of this method for enriching all types of components in a liquid, independent of their physical and chemical properties.

3.4 Influence of a Heated Airjet on Liquid Temperatures
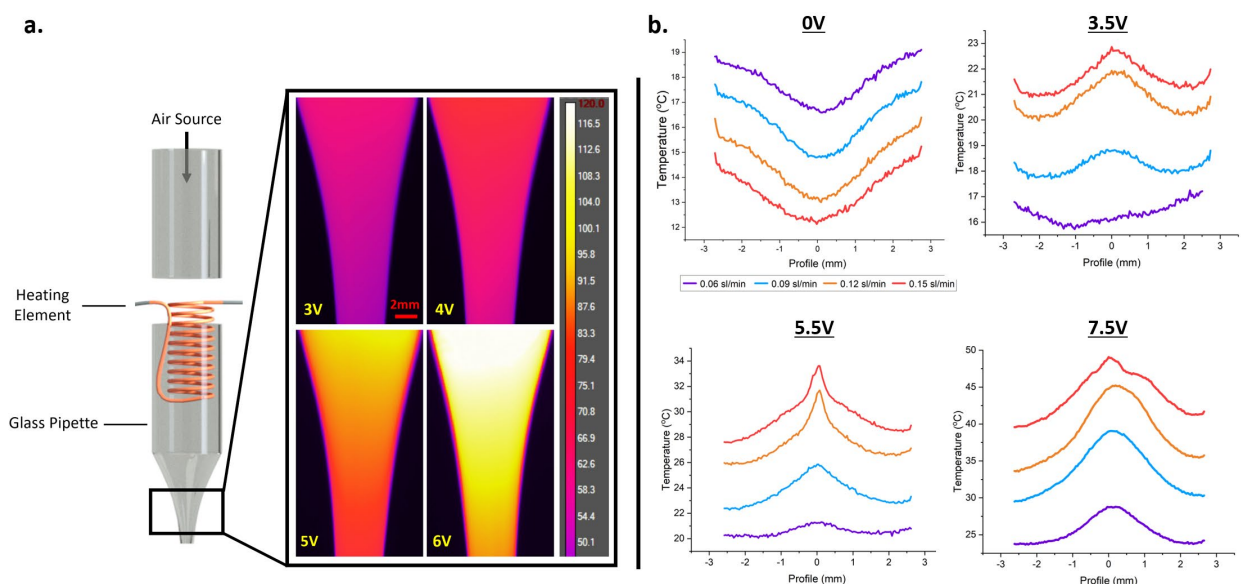
Figure 3.4 (a) Schematic of the heated airjet and associated thermal images taken at specified voltages. **(b)** Temperature profiles of the liquid surface for different voltages and airflow speeds.

The speed of the enrichment process is highly dependent on the evaporation rate underneath the airjet. To facilitate faster evaporation times, a heating element consisting of a nichrome coil was inserted and sealed in the glass pipette and connected to a variable voltage source as shown in **Figure 3.4 (a)**. A FLIR camera then measured the temperature changes near the pipette's exit nozzle at different voltages with a constant airflow rate of 1.0 sl/m. A linear relationship between the voltage and mean surface temperature was established (supplementary),

allowing for control over the airjet temperature. However, as the FLIR camera only monitors the temperature of the pipette exterior, the airjet temperature values are approximated.

To avoid damaging biological-based analytes that are vulnerable to denaturation or degradation at high temperatures [40,41], the liquid temperature was measured to determine how it was affected by airjet flow rate and temperature. In a 96-well plate, surface temperature profiles of a liquid solution containing methyl cellulose and tracking dye were monitored with the FLIR camera (**Figure 3.4 (b)**). When the nichrome heater is turned off (0V), faster airflow rates correspond to lower temperature minimums due to evaporative cooling [42] and quicker displacement of the boundary layer. However, this trend is reversed upon applying voltages greater than 3.5V to the heating element, whereby faster airflow rates caused higher peak temperatures through increased levels of heat transfer. However, voltages under 5.5V did not increase the temperature above 35°C despite the temperature readings in **Figure 3.4 (a)**, and therefore represented an upper limit to minimize degradation of biological analytes.

For the measured temperature profile at 0V, a negative temperature gradient can give rise to inward Marangoni flows due to the temperature-dependence of surface tension in the liquid [43]. In previous reports, Marangoni flows have been used to suppress the CRE by establishing a similar surface tension gradient through temperature differences or surfactants [44,45]. By controlling the heater temperature in the air path, we can control the liquid surface profile and achieve an almost isothermal profile. Since the effect of enrichment was observed under different temperature profiles, it can be concluded that the dominant effect responsible for analyte enrichment is the increased localized evaporation rate by jet air, while the surface-tension induced Marangoni flows play only a minor role. Therefore, the primary parameters we choose

in the following experiments will be air flow rate and air heating to achieve high enrichment efficiency within a short time and preserve the properties of the analytes for downstream process.

3.5 Double Stage Enrichment for Varying Sample Volumes

Figure 3.5. (a) Diagram of the two-stage enrichment process with images from certain steps labeled with red numbers. **(b)** Collection efficiency vs. time for λ-DNA for airjet enrichment (Enrich) and volume reduction (Evap [-]). **(c)** Comparison of ΔCq and collection efficiency for λ-DNA and HeLa-S3 RNA. **(d)** Cumulative ΔCq and fold-enrichment for λ-DNA, HeLa-S3 RNA, and heat inactivated SARS-CoV-2 after large volume (LV) and small volume (96) enrichment. **(e)** Cumulative ΔCq and fold-enrichment for negative controls using evaporative reduction only
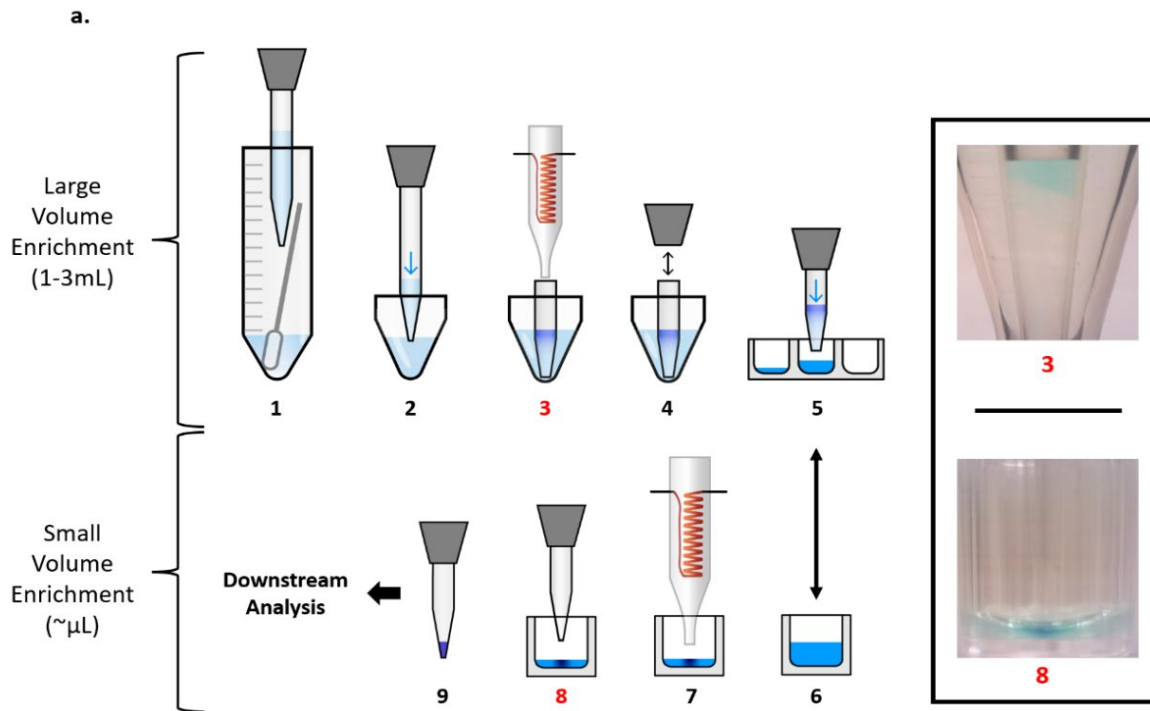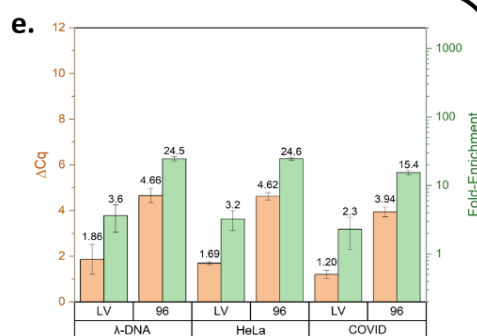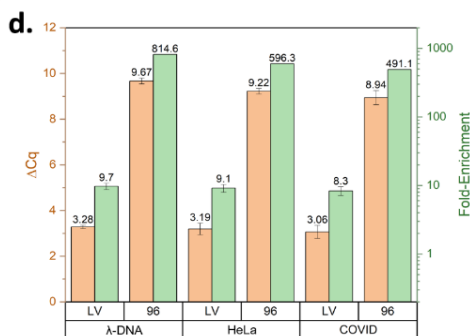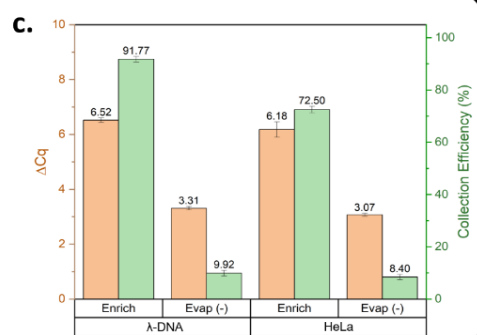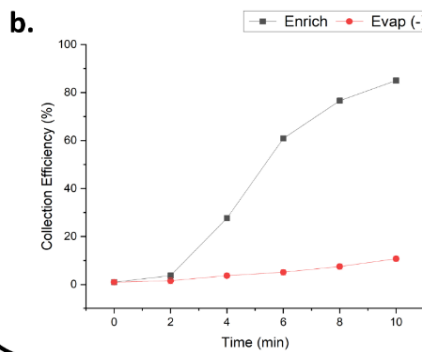
Incorporating airjet enrichment into the upstream steps of bioanalyte detection can significantly improve the sensitivity of testing methods. To demonstrate how airjet enrichment can be integrated to accommodate the fluid volumes typically used in these detection procedures, a model workflow was developed **(Figure 3.5 (a))**. The model comprises two stages of fluid processing, each corresponding to a range of fluid volumes that can be enriched. The first stage is the Large Volume Enrichment stage, which can enrich mesofluidic volumes, followed by the Small Volume Enrichment stage for enriching microfluidic volumes. Each step is optimized to balance enrichment speed and effectiveness to maximize the overall concentration of analyte prior to analysis.

The large volume enrichment stage is designed to process 1-3mL of fluid with an emphasis on maximizing the evaporation rate. This stage has a key component - the insertion of an inner tube (**Figure 3.5 (a), step 3**) where enrichment occurs. The enrichment can be visualized where the tube traps and localizes the enriched fluid, and eventually leads to the development of concentrated blue dye layer from the initially dilute dye solution (**Figure 3.5 (a), step 3**). The tube therefore acts similarly to the stabilizing properties of methyl cellulose, concentrating the enriched fluid while confining the airjet-induced shear forces. Although methyl cellulose can still be used, fluid turbulence is more likely to occur due to the larger container dimensions. This limits the airflow to a relatively small rate and leads to longer evaporation and processing times. The introduction of a physical barrier thereby raises the turbulence threshold, allowing stronger airflow rates to significantly improve the evaporation rate. In addition, the inner tube acts as a collection vessel which can be attached to a micropipette to transfer the enriched solution to the next stage (**Figure 3.5 (a), step 4-5**).

The small volume enrichment takes place in a 96-well plate and is designed to maximize the enrichment factor for microfluidic volumes. This stage utilizes methyl cellulose as the stabilizing additive and leads to the development of a highly concentrated spot after enrichment (**Figure 3.5 (a), step 8**). The effectiveness of airjet enrichment over conventional evaporative volume reduction is shown in **Figure 3.5 (b)** by tracking the collection efficiency for a λ-DNA solution over time. The collection efficiency is determined though qPCR by comparing the C_q values from 1uL of the original, unenriched sample with 1uL of the sample undergoing evaporation. The ΔC_q between these two samples is then applied to the original volume of 100uL to determine the percentage of functional analytes collected at the end of the sample preparation process (i.e. the end-to-end efficiency). According to the calculation, airjet enrichment which contained methyl cellulose was able to capture 85% of the λ-DNA in 1uL, while volume reduction without methyl cellulose could only capture 10%. The reason for this difference is that the airjet-enrichment localizes the analyte underneath the nozzle, making it easier to extract and transfer, while conventional evaporative volume reduction results in a uniformly distributed analyte. Therefore, demonstrating that airjet enrichment has a higher overall collection efficiency than conventional evaporation methods.

In addition to DNA, RNA is a frequently targeted analyte for detection but is also more susceptible to degradation. The collection efficiencies of HeLa-S3 RNA were therefore evaluated alongside λ-DNA to determine if airjet enrichment was equally as effective (**Figure 3.5 (c)**). Upon comparison, RNA results yielded consistently lower collection efficiencies averaging to 72%, while λ-DNA exhibited a 92% average collection efficiency. The reduced efficiency observed for RNA may be attributed to temperature-dependent auto-hydrolysis caused by the heated airjet. According to **Figure 3.4 (b)**, the voltage of 3.5V used during RNA enrichment

would yield a mild temperature profile. However, this profile measurement was taken with a filled well containing 350uL of liquid. It is likely that during the latter stages of RNA enrichment, the reduced fluid volume of ~20uL lowers the overall heat capacity and leads to increased temperatures. Therefore, while RNA enrichment did not achieve the same level of collection efficiency as DNA, it still demonstrated significantly higher efficiency than volume reduction-based enrichment.

To evaluate the effectiveness of the proposed workflow (**Figure 3.5 (a)**) in improving detection sensitivity, the large and small volume enrichment stages were combined and tested for three analytes: λ-DNA, HeLa-S3 RNA, and heat inactivated SARS-CoV-2. Cumulative ΔC_q and fold-enrichment values after each enrichment stage are shown in **Figure 3.5 (d)**. These values reflected the general purpose for each step concerning the optimization of fluid reduction and enrichment effectiveness. For the large volume stage, the enrichment could consistently reduce the C_q by an average of 3.17 cycles regardless of the nucleic acid tested. More importantly, this step could evaporate off 1mL of fluid and condense the analytes into 100uL for transfer. The small volume enrichment step then significantly reduced the overall C_q by an average of 9.27 cycles. Among the analytes, λ-DNA exhibited the highest ΔCq and fold-enrichment at 9.67 and 821.23x, respectively, while SARS-CoV-2 had the lowest values at 8.94 and 491.3-fold enrichment. RNA enrichment in general yielded lower values, consistent with the findings in **Figure 3.5 (c)**, and analyte loss occurred primarily during the small volume enrichment stage. These cumulative values can be compared to the negative trials in **Figure 3.5 (e)**, where the large volume stage lacked the inner tube, and the small volume stage did not include the methyl cellulose. Thereby solely relying on volume reduction to achieve enrichment. Based on this

69

difference, the airjet enrichment stages demonstrate considerable advantages to achieve analyte enrichment.

3.6 Co-Enrichment of PEG to Reduce Salt Concentration
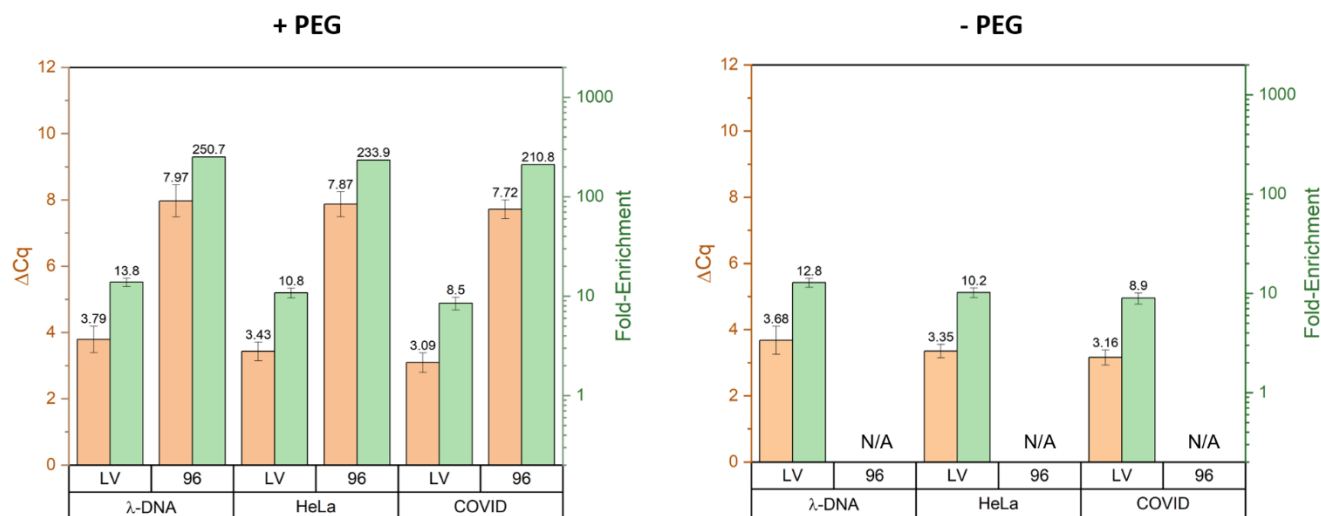
Figure 3.6. Series enrichment using samples spiked in 0.1mM EDTA. Enrichment values for each sample was compared with the co-enrichment of PEG (+ PEG) and the negative tests without PEG (- PEG).

While the series enrichment could improve the overall detection sensitivity, it did so using non-buffered solutions. However, many available storage solutions contain specific salts to prevent early degradation of the analyte – often in much higher concentrations than the analyte itself. As a key property of the airflow enrichment is the ability to enrich a wide range of substances, the co-enrichment of salt would be detrimental as it may interfere with downstream analysis, or the enrichment process itself. However, co-enrichment of other substances may be used to alleviate the salt buildup by creating a distinct environment which affects its solubility. PEG400 was used in the 96-well stage of the series enrichment of a buffered solution to

determine whether reduced salt co-enrichment would occur. Therefore, the prior series enrichment was repeated with the same analytes spiked in a solution of 0.1mM EDTA. EDTA is a chelator for divalent cations and a commonly used salt for RNA storage. However, it is also a PCR inhibitor at high concentrations as it sequesters the magnesium ions which are cofactors for polymerase activity. The presence of PEG400 was therefore examined to the degree by which it could reduce the ΔCq, while also recovering the signal during downstream analysis.

The cumulative enrichment values for λ-DNA, HeLa-S3 RNA, and heat inactivated SARS-CoV-2 in 0.1mM EDTA are shown in (**Figure 3.6**). The EDTA concentration threshold for qPCR functionality was determined to be 15mM when withdrawing 1uL of sample (supplementary). The effect of EDTA accumulation in downstream analysis is exemplified in the negative controls without the presence of PEG. While a qPCR signal was obtained after the large volume stage, the co-enrichment in the 96-well plate led to a high enough EDTA concentration to inhibit the PCR reaction – thereby leading to no signal. However, upon addition of a 5% PEG solution to the 96-well stage, recovery of the qPCR signal as well as enrichment was seen for all samples. Using the final λ-DNA fold-enrichment value of 250.7, it can be assumed that the EDTA would also be concentrated by the same amount if PEG was absent – crossing the 15mM threshold and resulting in no qPCR signal. The presence of a signal therefore indicates PEG of having some desalting capabilities.

The final ΔCq values were lower in the buffered samples compared those in the non-buffered samples. This reduction was caused by the addition of PEG, as it has surfactant-like properties which were believed to interfere with the methyl cellulose. Consequently, the enrichment efficiency is decreased as fluid turbulence becomes more prevalent in disrupting the formation of the enrichment spot. Therefore, while the addition of PEG reduces the co-

enrichment of salt, it also interferes with the airflow based CRE-reversal to some degree. Future studies which screen for an ideal compound which minimizes this trade-off would thus be beneficial.

3.7 Airjet Enrichment in ELISA
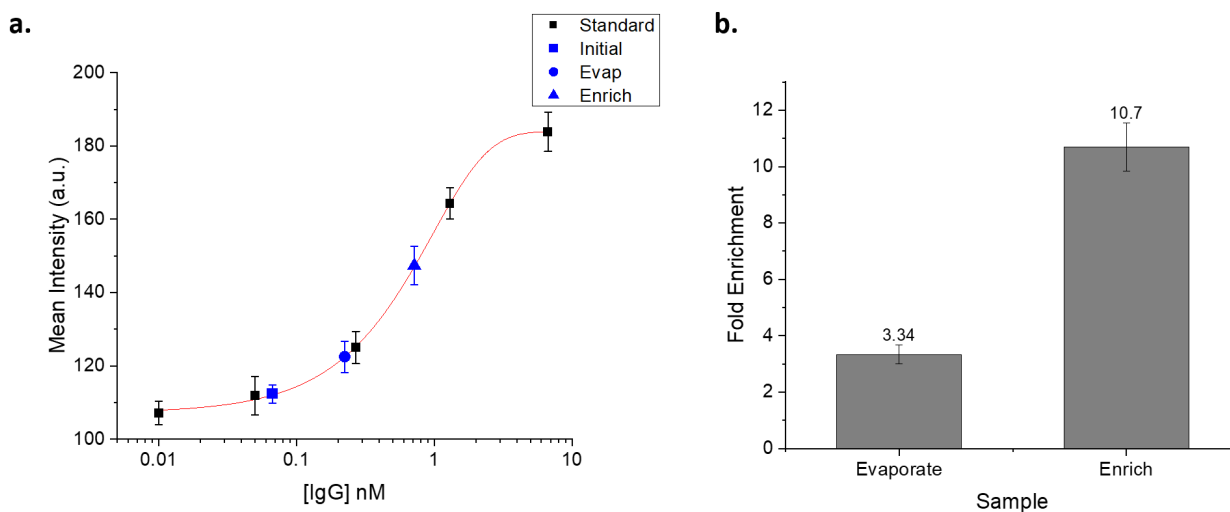
Figure 3.7. (a) Standard curve of ELISA assay (black) and respective concentrations of initial, evaporated, and enriched samples (blue). **(b)** Fold-enrichment values of evaporated and enriched samples.

Airjet enrichment was employed in a preliminary sandwich ELISA experiment to assess the fold-enrichment capabilities using rabbit IgG as a model antigen (**Figure 3.7a**). The enrichment of protein analytes poses a greater challenge as buffers with consistent salt concentrations are needed to preserve protein structure. To determine the effectiveness of enrichment, a comparison was made between a solution containing methyl cellulose（**Enrich in Figure 3.7 (a)**) and a negative control without methyl cellulose (**Evap in Figure 3.7 (a)**), where

the former was anticipated to undergo spot enrichment while the latter was expected to evaporate uniformly.

Although both samples improved the sensitivity of the assay, the fold-enrichment was lower than expected for each case (**Figure 3.7 (b)**), especially when compared to nucleic acid enrichment. In both cases, the salt concentration increases during antigen enrichment, which could potentially lead to its denaturation prior to binding with the capture antibody. Furthermore, in the enriched samples, the co-enrichment of salt may lead to the formation of density gradients that promote fluid flow, thereby disrupting the enrichment spot and impeding solute localization. Despite, the enriched sample enhancing the assay's sensitivity in comparison to the evaporated sample, this outcome may vary depending on the protein and its sensitivity to changes in salt concentration. Therefore, it is important to consider the interference of salt when determining the suitability of airjet enrichment in specific applications.

Methodology

3.8.1 Reagents

Methyl cellulose, carboxylate-modified red fluorescent 1um beads, EDTA, λ-DNA, and HeLa-S3 total RNA were purchased from MilliporeSigma. Heat inactivated SARS-CoV-2 were purchased from ATCC. FITC-labeled oligonucleotides and primers for λ-DNA, *BRACA1*, and *N1* were synthesized by Integrated DNA Technologies (IDT). For PCR analysis, iTaq Universal SYBR Green Supermix and iTaq Universal SYBR Green One-Step Kit were purchased from BioRad.

3.8.2 Fabrication of Nichrome Heater

A borosilicate glass pasteur pipette was separated into two halves. A coil from 40mm of 28-gauge nichrome wire was made and the ends braided with electrical wire. After the coil was inserted into the pipette half, the other half was re-sealed using a heat-resistant ceramic adhesive. The ends of the wire were connected to an adjustable DC voltage supply during operation.

3.8.3 Airflow Evaporation on a Sessile Droplet

Glass slides were treated under UV-Ozone for 10 minutes. A section of cured PDMS with a 14mm hole punched through the center was then pressed on the glass surface for a minute before removal to create a hydrophobic barrier. Solutions of the respective analyte were mixed in Ultrapure H_2O containing 50 ug/mL methyl cellulose. 20uL of the respective solution for enrichment was deposited on the hydrophilic section of the cover slip. The airjet nozzle was placed 5mm from the droplet surface and run for the designated amount of time.

3.8.4 Temperature Profiles for the Nichrome Airflow Heater

A FLIR thermal camera was used to capture thermal images for the nichrome heater and liquid in a 96-well plate. A solution of dye and 50 ug/mL methyl cellulose in Ultrapure H_2O was used as the bulk liquid and completely filled the well. The airflow rate and the voltages were adjusted accordingly. 3 minutes were given to achieve steady state before taking the temperature profile.

3.8.5 Enrichment in 96-well plate for DNA and RNA

Solutions containing dilutions of λ-DNA and 1:1000 HeLa-S3 total RNA were prepared in Ultrapure H_2O. Methyl cellulose was added to bring the concentration to 50ug/mL in addition to dilute tracking dye. For the reference sample, 1uL of each solution was transferred to a qPCR mixture with 10uL of total volume. The λ-DNA was enriched under the nichrome at a voltage of 3.25V and an airflow rate of 1.00 slpm. The enrichment was continued until the liquid height reached 10% of the original height and a concentrated dye spot formed. Upon completion, 1uL of fluid was extracted from the concentrated dye spot using a micropipette and deposited into a qPCR mix. The HeLa-S3 RNA solution was performed in a similar manner, except the airflow rate was reduced to 0.75 slpm when the liquid height reached 25% of original.

3.8.6 Double Stage Enrichment

To create the large volume container, the tops of a 15mL falcon tube were cut off at the 2.5mL mark and the bottom half was saved. A circular piece of foil containing an 8mm hole in the center was then adhered to the top of the tube. Solutions of diluted λ-DNA, HeLa-S3 RNA, and heat inactivated COVID-19 particles were made in Ultrapure H_2O containing a small amount of tracking dye. In the cut tube, 2mL of each solution was added. The ends of a pipette tip were trimmed, and the tip was placed in the hole. The nichrome nozzle was placed in the interior of the pipette tip and set at a flow of 2.0 slpm at a voltage setting of 7.5V. The enrichment was performed until 1mL had been evaporated off and a distinct layer of concentrated dye formed. The enrichment in the 96-well plate was performed as previously described, with the addition of 1uL of 5mg/mL methyl cellulose to the well to achieve spot enrichment. After enrichment in both the large volume and 96-well containers, 1uL of the enriched sample was transferred to a

qPCR reaction and compared with 1uL of reference sample from the initial nucleic acid solution. Negatives were run simply based on evaporation, where the inner tube was not present for the large volume enrichment, and no methyl cellulose was present in the 96-well enrichment.

3.8.7 Buffered Enrichment using PEG

Similar solutions of λ-DNA, 1:1000 HeLa-S3 RNA, and 1:500 of ATCC heat inactivated COVID-19 particles were made in 0.1mM EDTA with a small amount of blue tracking dye. The respective solutions were transferred to the large volume container and evaporated similarly to the original series enrichment. After formation of the enriched layer, 100uL of the layer was collected and deposited in a 96-well plate. In each individual well, 1uL of 5 mg/mL methyl cellulose and 5uL of PEG_{400} was added and mixed to form a homogenous solution. The enrichment was run according to the previous 96-well plate protocol.

3.9 Summary

In summary, we present an airflow-based method as a means of pre-concentration that can enrich a range of analytes to enhance downstream sensitivity in biosensors. The operation and mechanism of coffee-ring flow reversal was explored and applied to improve detection of biological analytes. Specifically, DNA, RNA, and viral particles were successfully enriched in common vessels used during nucleic acid testing. In addition, sample pre-treatment was also studied through the co-enrichment of PEG to reduce salt concentrations in buffered solutions. In addition to the simplicity of operation, the compatibility of airflow enrichment with standardized laboratory tools allows it to be easily integrated in various current procedures. Despite focusing

on nucleic acids in this study, airflow-enrichment can be extended to a multitude of different chemical and biological analytes for enhanced detection.

This chapter was based on the following paper: Edward Wang, Lousie C. Laurent, Drew. A. Hall and Yu-Hwa Lo, Sample preconcentration through airjet-induced liquid phase enrichment.

3.10 References

1. Lin, C. C., Hsu, J. L. & Lee, G. Bin. Sample preconcentration in microfluidic devices. *Microfluid. Nanofluidics 2010*, 2010 *103* **10**, 481–511

2. Giordano, B. C., Burgi, D. S., Hart, S. J. & Terray, A. On-line sample pre-concentration in microfluidic devices: A review. *Anal. Chim. Acta*, 2012 **718**, 11–24

3. Shen, M. *et al.* Recent advances and perspectives of nucleic acid detection for coronavirus. *J. Pharm. Anal.,* 2020 **10**, 97–101

4. Li, Z., Xu, X., Wang, D. & Jiang, X. Recent advancements in nucleic acid detection with microfluidic chip for molecular diagnostics. *TrAC Trends Anal. Chem.*, 2023, **158**, 116871

5. Broyles, B. S., Jacobson, S. C. & Ramsey, J. M. Sample filtration, concentration, and separation integrated on microfluidic devices. *Anal Chem*, 2003, **75**, 2761–2767

6. Yu, C., Davey, M. H., Svec, F. & Fréchet, J. M. J. Monolithic porous polymer for on-chip solid-phase extraction and preconcentration prepared by photoinitiated in situ polymerization within a microfluidic device. *Anal Chem* , 2001, **73**, 5088–5096

7. Dadfarnia, S. & Haji Shabani, A. M. Recent development in liquid phase microextraction

for determination of trace level concentration of metals—a review. *Anal Chim Acta*, 2010, **658**, 107–119

8. Shen, H., Fang, Q. & Fang, Z. L. A microfluidic chip based sequential injection system with trapped droplet liquid–liquid extraction and chemiluminescence detection. *Lab Chip*, 2006, **6**, 1387–1389

9. Sueyoshi, K., Kitagawa, F. & Otsuka, K. Recent progress of online sample preconcentration techniques in microchip electrophoresis. *J. Sep. Sci.* , 2008, **31**, 2650–2666

10. Manz, A. *et al.* Planar chips technology for miniaturization and integration of separation techniques into monitoring systems. Capillary electrophoresis on a chip. *J. Chromatogr. A*, 1992, **593**, 253–258

11. Tsuda, T., Nomura, K. & Nakagawa, G. Open-tubular microcapillary liquid chromatography with electro-osmosis flow using a UV detector. *J. Chromatogr. A,* 1982, **248**, 241–247

12. Fornells, E., Hilder, E. F. & Breadmore, M. C. Preconcentration by solvent removal: techniques and applications. *Anal. Bioanal. Chem.*, 2019, **411**, 1715–1727

13. Bacchin, P., Leng, J. & Salmon, J. B. Microfluidic Evaporation, Pervaporation, and Osmosis: From Passive Pumping to Solute Concentration. *Chem. Rev*, 2022, **122**, 6938–6985

14. Yang, M. *et al.* The application of coffee-ring effect in analytical chemistry. *TrAC Trends Anal. Chem.*, 2022, **157**, 116752

15. Garcia-Cordero, J. L. & Fan, Z. H. Sessile droplets for chemical and biological assays. *Lab on a Chip*, 2017, **17**, 2150–2166

16. Hua Hu, Larson, R. G. Marangoni Effect Reverses Coffee-Ring Depositions. (2006)

17. Mampallil, D. & Burak Eral, H. Historical perspective A review on suppression and utilization of the coffee-ring effect. *Adv. Colloid Interface Sci.*, 2018, **252**, 38–54

18. Erbil, H. Y. Evaporation of pure liquid sessile and spherical suspended drops: A review. *Advances in Colloid and Interface Science*, 2012, **170**, 67–86

19. Deegan, R. D. *et al.* Contact line deposits in an evaporating drop. *Phys. Rev. E - Stat. Physics, Plasmas, Fluids, Relat. Interdiscip. Top*, 2000, **62**, 756–765

20. Kim, S. J., Kang, K. H., Lee, J. G., Kang, I. S. & Yoon, B. J. Control of particle-deposition pattern in a sessile droplet by using radial electroosmotic flow. *Anal. Chem.*, 2006, **78**, 5192–5197

21. Mampallil, D., Eral, H. B., van den Ende, D. & Mugele, F. Control of evaporating complex fluids through electrowetting. *Soft Matter*, 2012, **8**, 10614

22. Zhang, J., Borg, M. K., Ritos, K. & Reese, J. M. Electrowetting Controls the Deposit Patterns of Evaporated Salt Water Nanodroplets. *Langmuir*, 2016, **32**, 1542–1549

23. Mampallil, D. *et al.* Acoustic suppression of the coffee-ring effect. *Soft Matter*, 2015, **11**, 7207–7213

24. Shilton, R., Tan, M. K., Yeo, L. Y. & Friend, J. R. Particle concentration and mixing in microdrops driven by focused surface acoustic waves. *J. Appl. Phys.*, 2008, **104**, 014910

25. Yen, T. M. *et al.* Reversing Coffee-Ring Effect by Laser-Induced Differential Evaporation. *Sci. Reports 2018 81*, 2018, **8**, 1–11

26. De Angelis, F. *et al.* Breaking the diffusion limit with super-hydrophobic delivery of molecules to plasmonic nanofocusing SERS structures. *Nat. Photonics*, 2011, **5**, 682–687

27. McLane, J. *et al.* Enhanced Detection of Protein in Urine by Droplet Evaporation on a Superhydrophobic Plastic. *Adv. Mater. Interfaces*, 2015, **2**, 1400034

28. Larson, R. G. Transport and deposition patterns in drying sessile droplets. *AIChE J.*, 2014, **60**, 1538–1571

29. Hua H., Larson, R. G. Evaporation of a Sessile Droplet on a Substrate, 2002

30. Shahraeeni, E., Lehmann, P. & Or, D. Coupling of evaporative fluxes from drying porous surfaces with air boundary layer: Characteristics of evaporation from discrete pores. *Water Resour. Res.*, 2012, **48**

31. Wang, E., Guo, Z., Tang, R. & Lo, Y.-H. Using airflow-driven, evaporative gradients to improve sensitivity and fluid control in colorimetric paper-based assays. *Lab Chip*, 2021

32. Behroozi, P., Cordray, K., Griffin, W. & Behroozi, F. The calming effect of oil on water. *Am. J. Phys.*, 2007, **75**, 407–414

33. Brisco, M. J. & Morley, A. A. Quantification of RNA integrity and its use for measurement of transcript number. *Nucleic Acids Res.*, 2012, **40**, e144–e144

34. Fleige, S. & Pfaffl, M. W. RNA integrity and the effect on the real-time qRT-PCR performance. *Mol. Aspects Med.*, 2006, **27**, 126–139

35.   Xu, X. & Ma, L. Analysis of the effects of evaporative cooling on the evaporation of liquid droplets using a combined field approach. *Sci. Reports 2015 51*, 2015, **5**, 1–6

36.   Trantum, J. R., Baglia, M. L., Eagleton, Z. E., Mernaugh, R. L. & Haselton, F. R. Biosensor design based on Marangoni flow in an evaporating drop. *Lab Chip*, 2014, **14**, 315–324

37.   Still, T., Yunker, P. J. & Yodh, A. G. Surfactant-Induced Marangoni Eddies Alter the Coffee-Rings of Evaporating Colloidal Drops. *Langmuir*, 2012, **28**, 4984–4988

38.   Kim, C. W., Someren, J. T., Kirshen, M. & Rha, C. Steric Exclusion of Salts by Polyethylene Glycol. *Phys. Chem. Liq.*, 1988, **18**, 11–20